catalysts

MDPI

Article

High-Performance Hydrogel Based on Modified Chitosan for Removal of Heavy Metal Ions in Borehole: A Case Study from the Bahariya Oasis, Egypt

Mohammed F. Hamza [1,2,*], Saad H. Alotaibi [3], Yuezhou Wei [1,4,*] and Noha M. Mashaal [5,*]

1 School of Nuclear Science and Technology, University of South China, Hengyang 421001, China
2 Nuclear Materials Authority, El-Maadi, Cairo 11728, Egypt
3 Department of Chemistry, Turabah University College, Taif University, Taif 21944, Saudi Arabia; s.alosaimi@tu.edu.sa
4 School of Nuclear Science and Engineering, Shanghai Jiao Tong University, Shanghai 200240, China
5 Department of Geology, Faculty of Science, Menoufia University, Shibin El-Kom 32511, Egypt
* Correspondence: m_fouda21@hotmail.com (M.F.H.); yzwei@sjtu.edu.cn (Y.W.); noha.mashal@science.menofia.edu.eg (N.M.M.); Tel.: +20-111-668-1228 (M.F.H.); +86-771-322-4990 (Y.W.); +20-100-305-1898 (N.M.M.)

Abstract: Globally, there is a rising demand for water purification. This demand is driven by numerous factors, including economic growth, increasing population, water shortage, and deterioration of water quality. The current work highlights the manufacturing of environmentally friendly and highly efficient sorbent based on chitosan nanoparticles after successive crosslinking (using glutaraldehyde) and modification through grafting of 4-aminoazobenzene-3,4′-disulfonic acid (AZDS) as a source of sulfonic groups. First, the produced sorbent was thoroughly specified using FTIR, TGA, SEM, SEM-EDX, pH_{pzc}, BET (nitrogen sorption desorption isotherms), and elemental analyses (EA). The sorbent was tested for the sorption of Fe(III) before application to highly contaminated iron water well samples. Next, the sorption was improved as the sulfonation process was conducted under the selected experimental conditions within 25 and 20 min with a maximum capacity of 2.7 and 3.0 mmol Fe g^{-1} in visible light and under UV, respectively. Then, the uptake kinetics for both techniques were fitted by the pseudo-first-order rate equation (PFORE), in which the effect of the resistance to intraparticle diffusion has remained an unneglected factor, while the Langmuir equation has fitted the sorption isotherms. After that, the efficient desorption was achieved by using 0.2 M hydrochloric acid solution, and the desorption process was as fast as the sorption process; 15 min was sufficient for complete desorption. The sorbent shows high selectivity for heavy metal ions compared to the representative elements. Finally, the sorbent was used for the removal of heavy metal ions from a highly contaminated water well in the Bahariya Oasis and appeared to be highly efficient for heavy metal removal even in a diluted solution. Accordingly, it can be implemented in the task of water treatment.

Keywords: water treatment; decontamination; heavy metal removal; Bahariya Oasis; eco-friendly adsorbent

check for updates

Citation: Hamza, M.F.; Alotaibi, S.H.; Wei, Y.; Mashaal, N.M. High-Performance Hydrogel Based on Modified Chitosan for Removal of Heavy Metal Ions in Borehole: A Case Study from the Bahariya Oasis, Egypt. *Catalysts* **2022**, *12*, 721. https://doi.org/10.3390/catal12070721

Academic Editor: Roberto Fiorenza

Received: 25 May 2022
Accepted: 27 June 2022
Published: 30 June 2022

1. Introduction

Water is becoming drastically scarce, and the supply of safe water has become a global challenge. Freshwater comprises only 0.003% of the world's total water bodies. Furthermore, groundwater accounts for more than 95% of the available liquid freshwater constituting 30.1% of the total fresh water on earth [1,2]. In Africa, freshwater resources are exceptionally vulnerable to variable natural and anthropogenic factors. The current efforts to mitigate shocks and pressures on water resources are unsuccessful. This issue needs an early and comprehensive response from the African countries in order to reduce both ongoing and future impediments [3–6]. Clean drinking water is indispensable for healthy

living, but the access to uncontaminated water is apprehensive. Every year, water pollution-related diseases account for the death of around 3,575,000 people. Today over 2 billion people are facing water shortage with inadequate (insufficient and/or contaminated) water supply. The current number is projected to reach 6 billion people by 2050 [7,8]. Thus, providing clean water is the sixth goal of the 17 s Sustainable Development Goals (SDGs) [9].

Egypt is one of the water-stressed countries, which faces many obstacles, including limited water resources, a fast-growing population, intensive agriculture practices, vulnerability to climatic changes, and the construction of the Grand Ethiopian Renaissance Dam (GERD) [10,11]. The induvial per capita share of water has been lowered under the water scarcity limit since decades. Nowadays, individual water consumption has been decreased to reach 560 m^3/yr [12]. Hence, the country has witnessed a growing interest in the management of water resources with a special focus on groundwater treatment and desalination. Egypt's 2030 National Water Vision and future development plan is to secure basic needs (water, energy, and food) for the public, including the reclamation of 4×10^6 feddans that depends mainly on groundwater. In this aspect, the Bahariya Oasis is one of the targeted reclaimed areas. The Bahariya Oasis is famous for iron ore mining, dates, olive oil, and tourism. It is one of several urban oases in the Western Desert of Egypt, where groundwater is the sole source of water used for both domestic and agricultural purposes. Also, groundwater is becoming more important as an alternative source of water supply, and it contributes 2 BCM/yr abstracted from the Western Desert and Sinai (non-renewable) [13]. The budget of groundwater influences the availability of drinking water, food and energy security, and ecological community. However, the replenishment of groundwater over the longevity of humans is finite and represents only 6% of the total groundwater residing in the upper crust [14]. Groundwater is essentially susceptible to pollution, which can be triggered by natural and/or anthropogenic factors. Several factors control the salinity of the aquifer, including the rate of recharge, the rates and distribution of precipitation, flow velocity, nature of discharge areas, kind of aquifer material, and residence time [15]. Both geological and hydrogeological settings have a profound impact on groundwater by controlling water quality and directions of water flow [16]. Many places in the Western Desert are liable to seasonal variation in groundwater levels and excessive rapid increase in TDS (salinization), which are linked to excessive water pumping and agro-activity resulting from the expansion of the reclaimed areas [17].

Heavy metals are one of the most common water contaminants, especially in groundwater coupled with fertilizers that are largely used in agricultural practices. Iron (Fe) is one of the foremost considerable components of the soil and rocks, representing around 5% of the earth's crust. It is the second most abundant metal on the earth's crust after aluminum [18]. The weathering of iron-bearing minerals is a substantial source of iron in groundwater [19]. The liability and susceptibility of pollutants to make contact with groundwater mark its vulnerability to contamination. Herein, the rock material of the groundwater aquifer has the ability to dissolve, resulting in a notable concentration of iron in the Nubian Sandstone Aquifer System (NSAS) [20]. The concentrations of trace elements in groundwater can vary significantly. The notable similarity of trace elements between the aquifer rocks and water samples in the order of Fe > Zn > Mn suggests a lithogenic origin. The standard permissible limits for iron, manganese, and zinc in drinking water are 0.3 ppm, 0.05 ppm, and 0.05 ppm, respectively [21]. However, the studied groundwater samples substantially cross the permissible limits.

Various techniques have been implemented to remove contaminants from polluted water and effluent solution, including nanofiltration, chemical precipitation [22–27], solvent extraction [28,29], chelating resins [30–35], ion-exchange [36–38], biosorption [39–41], adsorption [34,42–44], and many other applications have been implemented to remove contaminates from polluted water [45,46].

Biopolymers sustain supremacy over other synthetic polymeric substances as they are environmentally friendly [47–50]. Several chitosan-based biomaterials have been applied with promising results [51–54].

Different sorbents were tested for Fe(III) and other heavy metal removal [55–57]. New types of carbon-based nanomaterials have been developed as carbon dots(CDs) for the detection of heavy metals and drug delivery [58]. On the other hand, some other sorbents bearing oxygen, sulfur, and nitrogen functional groups were used for efficient removal of iron and other heavy metals, such as peptide sorbent [59], poly(gamma-glutamic acid) functionalized with Fe_3O_4-GO-(o-MWCNTs) [60], thiol functionalized polymer [61], and functionalized silica particles with amine-terminated PAMAM dendrimer, which show a high affinity for Fe(III) and Ag(I) adsorption from DMF solution [62].

In this paper, we focus on the application of bio-based material to groundwater treatment in highly contaminated water wells from the Bahariya Oasis, Egypt. The sorption properties of the chitosan composites can be improved by grafting new groups containing sulfonic and amine moieties to increase the density of functional groups for variety in the binding mechanism and improve the sorption selectivity. The sorbents were firstly characterized by a wide range of analyses, i.e., FTIR, TGA, SEM, SEM-EDX, pH_{pzc}, BET (nitrogen sorption desorption isotherms), and elemental analysis (EA), before investigating the sorption toward Fe(III) ions in visible light and under UV effect, and removal of contaminants from the groundwater samples from the Bahariya Oasis.

2. Results

2.1. Characterization of Sorbent

2.1.1. Physical Characterization

The SEM analysis displays the particle size with the surface image; the average diameter, as shown in Figure 1, is around 34 ± 0.5 µm for CH particles. While this size is not significantly affected by the grafting process, which shows the average diameter around 37.5 ± 0.5 µm after the functionalization of chitosan (for CH-AS), the EDX analysis represents the S element on the sorbent after sulfonation as well as increasing the O and N ratios from 45.57 and 4.28, respectively, to 48.4 and 5.97, respectively. This verifies the successive grafting of the sulfonating moieties on the activated chitosan particles.

The textural properties show that the sorbents are porous, and the functionalization sorbent is much higher than the crosslinked chitosan: the specific surface of CH is close to 23.2 $m^2\ g^{-1}$; while the mesoporous volume is mainly around 0.029 $cm^3\ g^{-1}$, these ratios reached 30.4 $m^2\ g^{-1}$ and 0.033 $cm^3\ g^{-1}$, respectively.

2.1.2. Chemical Characterization

Elemental Analyses

The elemental analyses for C, N, H, and S are reported in Table 1. The functionalized composite increases the N content to 4.312 mmol from 3.39 mmol of the crosslinked chitosan. This is mainly due to the azid groups of the grafted moiety. On the other side, the fraction of S is close to 0.7112 mmol for the CH-AS. This is derived from the sulfonic groups from the grafted moiety. Moreover, the increase in the O fraction of the functionalized composite to that of pristine crosslinked particles verifies the success of grafting the sulfonic groups on the chitosan surface.

Table 1. Elemental analyses (C, N, H, O, and S) of the CH and CH-AS sorbents.

Sorbent	C	N	H	O	S
CH: (%)	46.75	4.75	7.02	41.48	0
CH: mmol	38.923	3.3914	69.65	25.927	0
CH-AS: (%)	42.85	6.04	6.55	42.28	2.28
CH-AS: mmol	35.676	4.312	64.987	26.427	0.7112

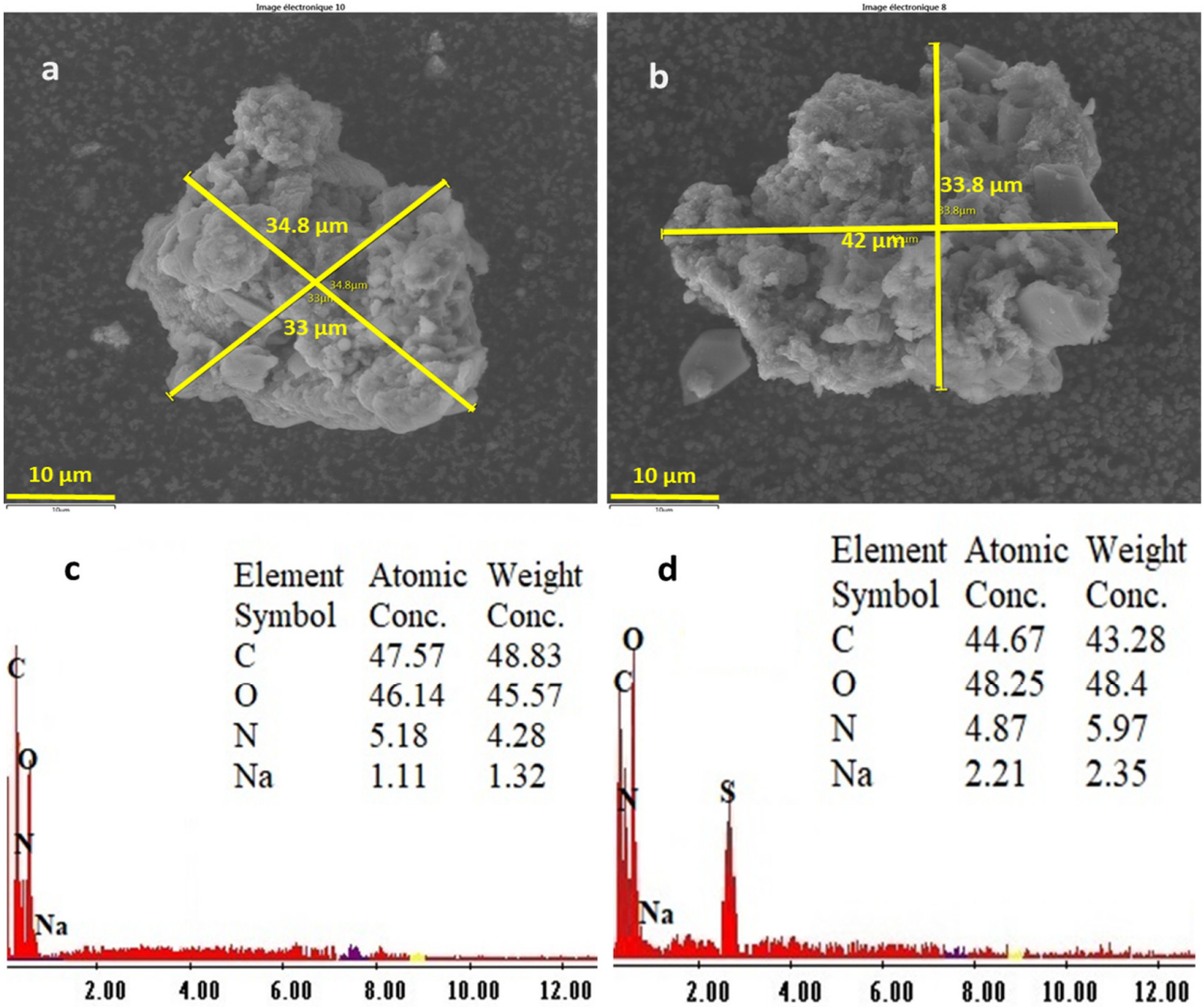

Figure 1. SEM analysis of crosslinked chitosan and sulfonated functionalized composite (**a**,**b**) and with EDX characterization of both sorbents (**c**,**d** respectively).

FTIR Spectroscopy

FTIR spectroscopy confirms that the modification is achieved on the chitosan (Figure 2 (for 4000–400 cm^{-1} wavenumber) and Figure S1 (for 1800–400 cm^{-1} wavenumber)); furthermore, Table 2 reports the detailed assignment of the most significant peaks.

The sulfonation of pristine chitosan shows a series of changes as follows:

(a) Appearance of a peak at 3068 cm^{-1} for CH str. of the aromatic ring from the grafted moiety;
(b) The peak is close to 1720 ± 5 cm^{-1}, which is assigned to C=C of Comb. aromatic bands (sh.) from the grafted moiety;
(c) Peak at 795 cm^{-1} for CO wag. Out-of-phase, skeletal vibration;
(d) Appearance of the peaks in the range of 686 cm^{-1} for N-C-N in-plane bending, for attaching the amine groups with the chitosan moiety;
(e) Appearance of a peak at 618 for -S-O str. of the grafted sulfonic group.

Additionally, the intensity of some peaks is changed while the grafting was performed, which means that it could affect the environment of these groups as the intensity of the NH str. peak at 3459 cm^{-1}. Moreover, most of these peaks are shifted and decreased in intensity while the metal ions are being adsorbed.

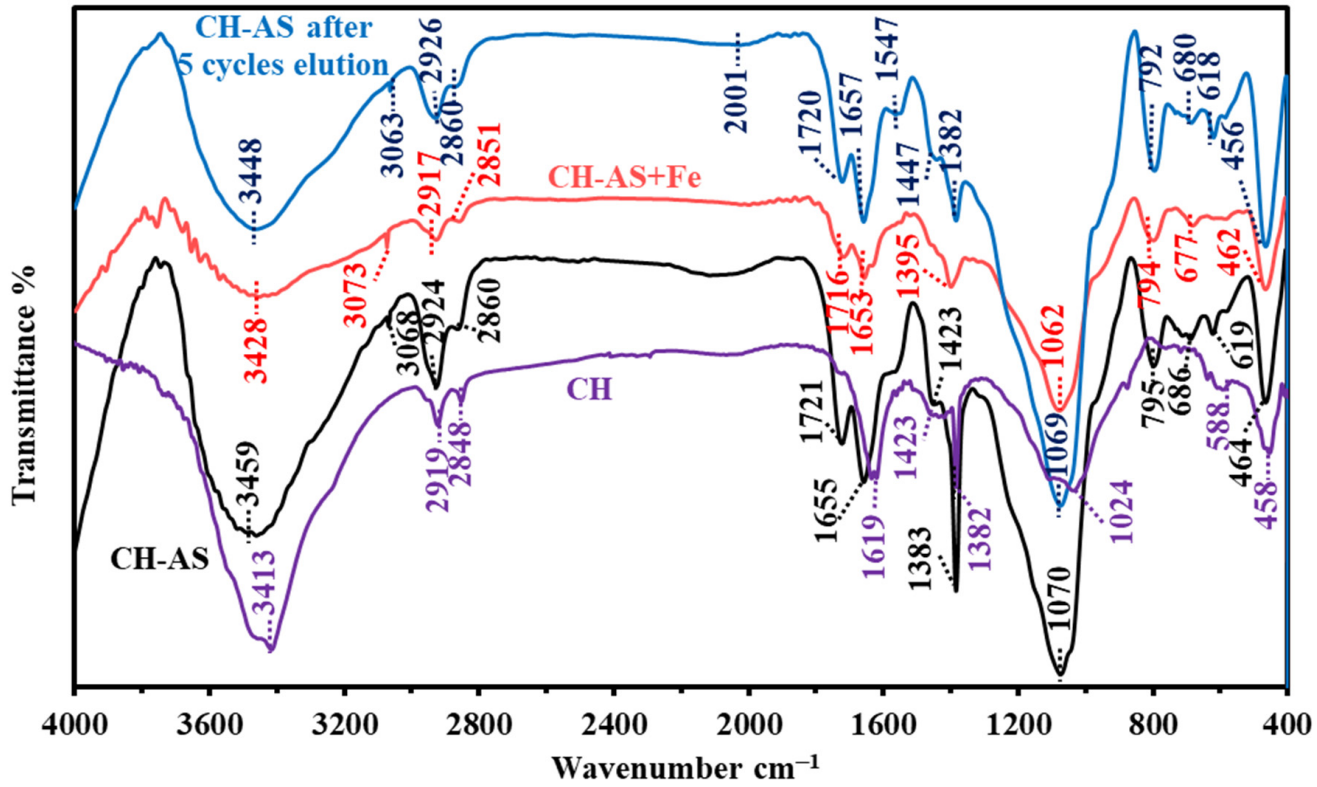

Figure 2. FTIR characterization of CH, CH-AS, after loading by Fe(III) and after the 5th cycle of sorption/desorption (scale 400–4000 cm^{-1}).

Table 2. FTIR assignment peaks for the CH, CH-AS, after loading by Fe(III) and after the 5th cycle of sorption/desorption.

Assignment	CH	CH-AS	CH-AS+Fe	CH-AS 5th Cycles	Ref.
N-H and OH str.	3413	3459	3428	3448	[63,64]
Aromatic CH str.		3068	3073	3063	
Aliphatic C-H str.	2919, 2848	2924, 2860	2917, 2851	2926, 2860	[65,66]
Comb. aromatic bands (sh.)		1721	1716	1720	[66]
C=O C=C(aromatic) and C=N str. N-H bend and open-chain azo (-N=N-)	1619	1655	1653	1657	[63,64,67]
C-N/C-C str., and CH_2 bend	1423	1423	1395	1447	[63,64,68–70]
Secondary amine	1382	1383		1382	[66]
C-O-C asymm./C-O str. and NH_2 rock.	1024	1070	1069	1062	[71]
Aromatic C-H bend (in-plane)					[63]
NH_2/CO wag. Out-of-phase		795	794	792	[63,66]
N-C-N in-plane bending		686	677	680	[68,69]
O- H bend out-of-plane, C-H (def.), and -S-O (str.)	588	618		618	[66]
C-S (str.)	458	464	462	456	[72,73]

TGA Analysis

The thermal degradation of the functionalized composite is reported in Figure 3. Three weight loss stages are noticed, while the total weight loss is around (85.1%) associated with the bound water loss at the composite surface and from the porous network. It is worth

noting that the weight loss was measured until 900 °C, in which, from 700 °C, the sorbent particles were completely degraded.

The major three degradation steps are identified as follows:

(a) The water loss (from the surface or porous) is assigned to 211.21 °C. The total loss at this stage is around 28.9%;
(b) Between 211.21 and 472.21 °C (additional loss: ≈ 40.575%), this stage is defined by the degradation and depolymerization of carbohydrates in the polysaccharide moieties and that of reactive groups (amines and hydroxyls) depolymerization of the polymers;
(c) Above 472.21 °C and up to 900 °C (additional loss: ≈ 15.637%), which is attributed to the decomposition of the rest of the organic functional groups and the degradation of the polymer char. Several waves in the dTGA spectrum, as reported in Figure S2, were identified at 85.62, 337.4, 574.6, and 740.2 °C.

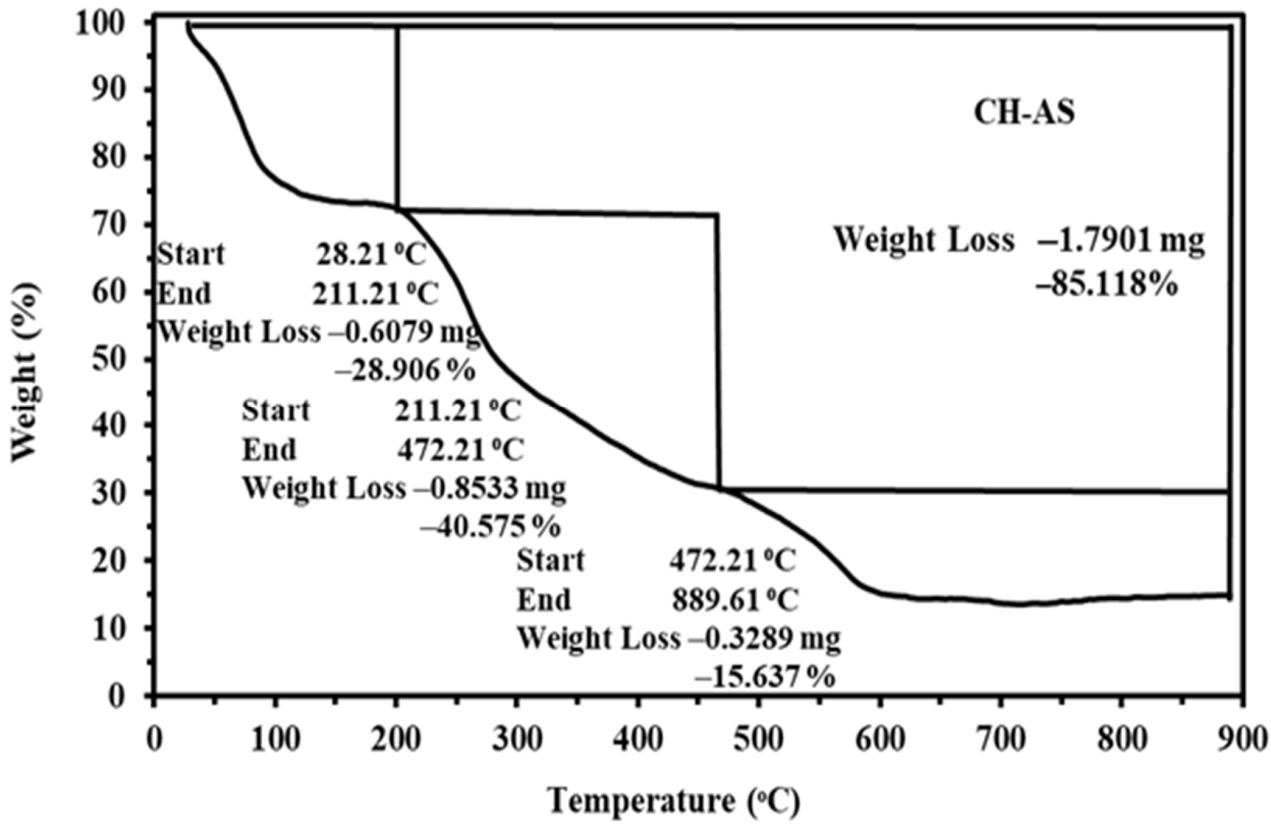

Figure 3. TGA of the functionalized chitosan composite.

pH_{PZC}

The pH_{PZC} of the prepared sorbents (crosslinked chitosan and sulfonated composites) was close to 6.69 and 5.344, respectively, as shown in Figure 4. Chitosan-bearing amine and hydroxyl groups shift the pK_a on the basic side, while the sulfonated groups (in the CH-AS) have an acidic character and shift the pK_a values to the acidic direction. Hamza et al. reported the pH_{pzc} of different composites based on biopolymers in the range of 2.84 and 4.82 [34,74–76] from 0.1 M NaCl solutions. Sulfonation causes a strong shift in the $pH_{PZC,}$ as noticed in sulfonation of some agriculture wastes (hawthorn kernel), which were shifted from 7 to 3.9 [77]. Urbano and Rivas reported that [78] pH_{PZC} is close to 3.4 for montmorillonite polystyrene sulfonate-polyacrylamide glycolic composite.

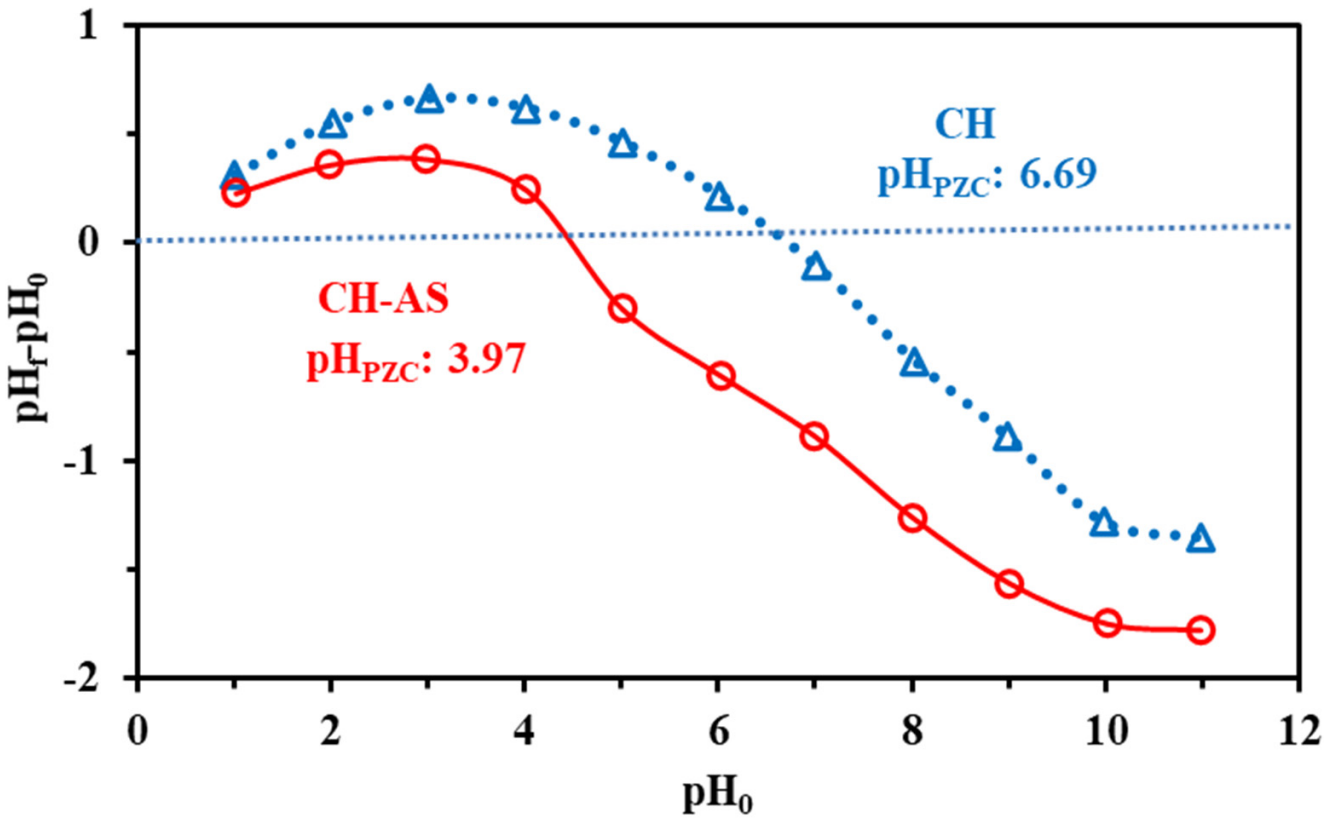

Figure 4. The pH_{pzc} characterization of crosslinked and functionalized chitosan composites.

2.2. Sorption Properties

2.2.1. pH Effect

Figure 5 shows the effect of the pH of the solution on the sorption of Fe(III) for both CH and CH-AS sorbents in visible light and under UV conditions. The crosslinked chitosan exhibits a little sorption affinity on Fe(III) compared to CH-AS sorbent under the same experimental conditions. The CH and CH-AS sorbents show average sorption capacities of 1.6 and 2.1 mmol g^{-1} for CH at light and UV, respectively, while the capacity has increased to 2.72 and 3.08 mmol g^{-1} for CH-AS at light and UV, respectively. From Figure 5, the triplicated experiments verify the reproducibility of the sorbents and the efficient uses of UV for improving the sorption capacities. Regardless of the equilibrium pH (in the range of 1 to 3.5 and below the precipitation point of iron. The sorption capacity for both sorbents was low at acidic pH values (1 and 2). This is due to the protonation of reactive groups that make repulsions with positively charged metal ions and consequently decrease the sorption capacity. As pH increases, the protonation of reactive groups becomes decreased to pH 6.69 and 3.97 for CH and CH-AS, respectively (the pH_{pzc} levels, which convert to completely negative charge), depending on increasing the sorption capacity. It is noticed that at pH_{eq} close to 3.1, the sorption capacity remains high for CH-AS (2.8 $\pm$ 0.25 mmolg^{-1}), while the sorption remains increased with the pH for CH sorbent and the maximum sorption capacity is around 1.5 $\pm$ 0.1 mmol g^{-1} at pH_{eq} 3.7. Figure S3a,b shows the variation of the pH values during sorption for CH and CH-AS at different light moods: the change of pH does not exceed 0.5 and 0.3 for CH and CH-AS sorbents.

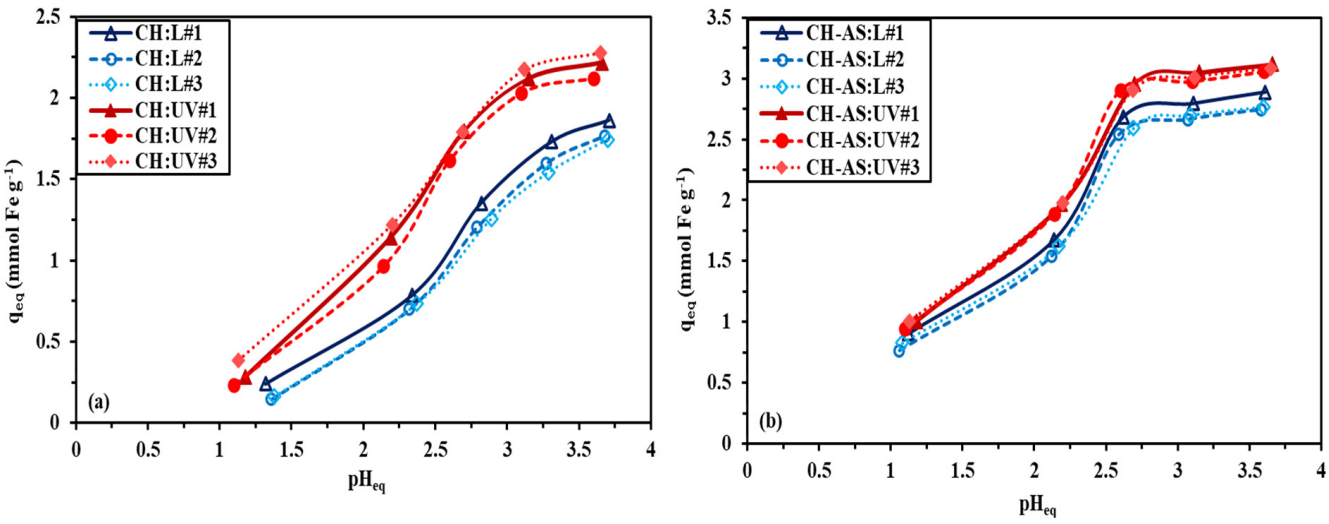

Figure 5. Effect of pH on sorption capacity for CH (**a**) and CH-AS (**b**) under light and UV.

2.2.2. Uptake Kinetics

Under the selected experimental conditions (i.e., C_0: ≈ 1.7 (±0.1) mmol Fe L^{-1}; pH_0: 3.0; SD: 0.5 g L^{-1}), the sorption of Fe(III) on the CH-AS is a fast phenomenon in which the equilibrium is reached within 35 min. Different sorption mechanisms are assigned as the mass transfer (i.e., resistance to film, bulk, and/or intraparticle diffusion) as well as proper reaction rates [79].

The speed of agitation is sufficient to limit the resistance to bulk diffusion. In addition, minimizing the effect of resistance to film diffusion and yet is not neglected. Different mechanisms were used for fitting the kinetic profiles, i.e., PFORE—pseudo-first-order rate equation (Figure 6), PSORE—pseudo-second-order rate equation (Figure S4a) [80], and RIDE—resistance to intraparticle diffusion (Crank equation, Figure S4a) [81] in light and UV, respectively. For evaluating the different mechanisms, Table 3 reports the parameters of each model (including the coefficients of the relevant fits). The PFORE successfully fits the experimental data in both conditions better than the other models: this was achieved by matching both the calculated and experimental values for the q_{eq} and R^2, which provide priority to the PFORE over the PSORE and RIDE. The PFORE model is described as a physical-type interaction, which is associated with the ion-exchange mechanism.

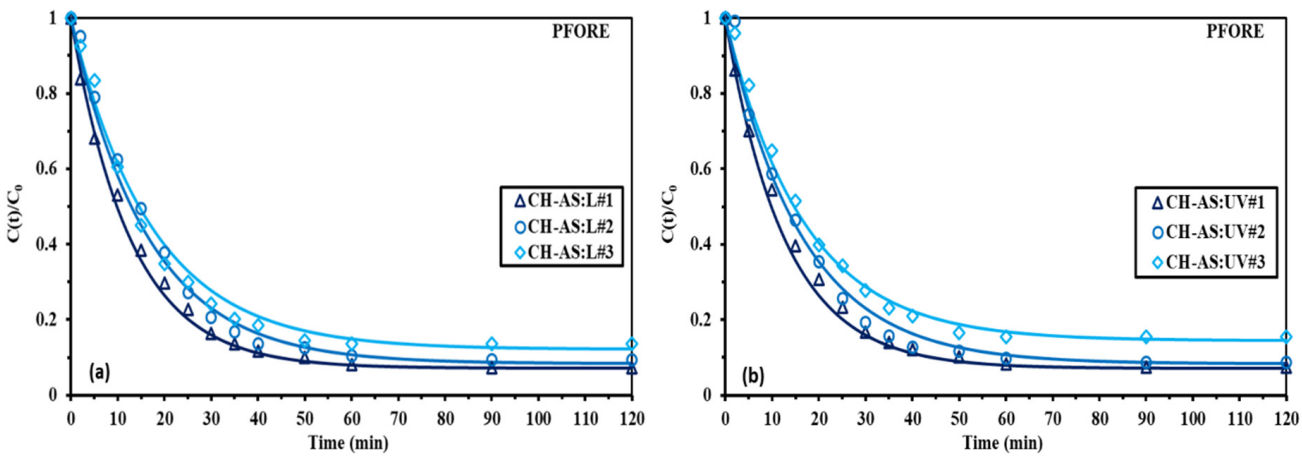

Figure 6. Uptake kinetics (PFORE) in light (**a**) and under UV condition (**b**).

Table 3. The parameters of the models for Fe(III) uptake kinetics.

		Visible Light (L)			Ultra Violet		
Model	**Parameter**	**#1**	**#2**	**#3**	**#1**	**#2**	**#3**
Exp.	q_{eq} (mmol Fe g^{-1})	2.69	2.71	2.78	3.12	3.06	3.14
PFORE	$q_{eq,1}$ (mmol Fe g^{-1})	2.65	2.77	2.81	3.16	2.99	3.11
	$k_1 \times 10^2$ (min^{-1})	2.18	2.11	3.92	5.93	6.72	6.92
	R^2	0.983	0.988	0.989	0.992	0.989	0.991
	AIC	−98.77	−78.9	−101.1	−104.5	−95.8	−112.3
PSORE	$q_{eq,2}$ (mmol Fe g^{-1})	1.87	2.48	2.22	2.37	2.61	2.69
	$k_2 \times 10^2$ (L $mmol^{-1}$ min^{-1})	3.87	2.96	1.99	9.85	12.4	15.8
	R^2	0.795	0.801	0.881	0.816	0.875	0.881
	AIC	−21.1	−36.55	−41.43	−76.3	−73.2	−58.6
RIDE	$D_e \times 10^8$ (m^2 min^{-1})	1.11	2.18	1.65	1.75	1.16	1.59
	R^2	0.899	0.917	0.879	0.942	0.939	0.967
	AIC	−65.44	36.4	−33.2	−92.9	−98.0	−101.4

2.2.3. Sorption Isotherm

The distribution of Fe(III) between the solid and the liquid phases at pH_0 3 ± 0.05 (in which the pH_{eq} was around 3.1 ± 0.03) was represented through the sorption isotherm (Figures 7 and S5). The model was fitted in the three repeated experiments for reproducibility. The Langmuir, Sips, and Freundlich are the three model equations that are used for fitting the experimental data using parameters that are reported in Table 4, which shows an extensive increase in the sorption capacity before reaching saturation with the equilibrium concentration of 4.6 ± 0.15 mmol Fe(III) g^{-1}. The fitted models are not parallel with the Freundlich equation (power-type equation) and are more fitted with the Langmuir and Sips (overlapped). The maximum capacity of saturation for the monolayer (i.e., $q_{m,L}$) is around 4.52 mmol Fe g^{-1}, a little lower than that of the maximum experimental capacity (i.e., 4.551 mmol Fe g^{-1}).

Table 5 reported the sorption comparison properties of a series of alternative sorbents in the literature toward Fe(III). Taking into account the pH and temperature of the sorption environment, the CH-AS is considered the highest sorption to Fe(III) with fast kinetic properties. Most of these sorbents were tested against Fe(III) at pH (4–7).

Table 4. Modeling of Fe(III) sorption isotherms.

Model	**Parameter**		**1**	**2**	**3**	**1**	**2**	**3**
Experimental	$q_{m,exp.}$	mmolFeg^{-1}	4.773	4.528	4.352	5.04	5.32	4.99
Langmuir	$q_{m,L}$	mmol Fe g^{-1}	4.711	4.498	4.361	4.98	5.27	5.04
	b_L	L $mmol^{-1}$	1.97	1.53	1.68	2.65	3.11	2.95
	R^2	-	0.963	0.954	0.971	0.994	0.982	0.988
	AIC	-	−154.5	−148.5	−166.9	−132.5	−171.4	−147.3
Freundlich	k_F	$mmol^{1-1/n}$ g^{-1} $L^{1/n}$	0.60	0.75	0.89	0.81	0.62	0.72
	n_F	-	2.18	2.22	2.16	1.87	2.55	3.01
	R^2	-	0.901	0.895	0.883	0.836	0.799	0.816
	AIC	-	−38.6	−42.1	−48.3	−21.1	−36.5	−32.2
Sips	$q_{m,S}$	mmol Fe g^{-1}	4.75	4.541	4.366	5.17	5.41	5.04
	b_S	L $mmol^{-1}$	0.89	0.91	0.94	0.989	0.982	0.981
	n_S	-	1.53	1.64	1.12	2.18	2.11	1.84
	R^2	-	0.998	0.960	0.988	0.994	0.981	0.993
	AIC	-	−132	−144	−135	−122.1	−154.3	−137.2

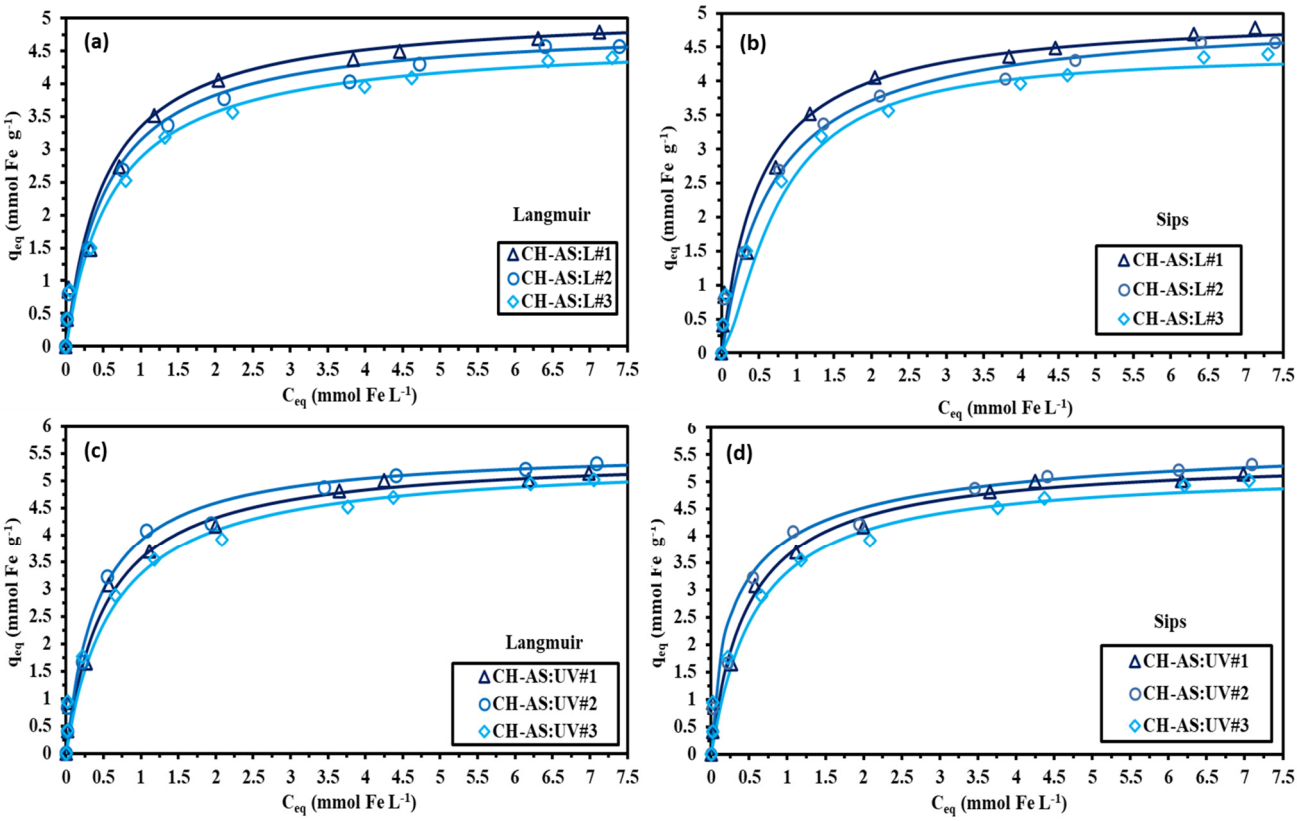

Figure 7. Sorption isotherms for fitting the experimental data of Fe(III) sorption by Langmuir (**a**,**c**) and Sips (**b**,**d**) at light and UV effects.

Table 5. Comparison of alternative sorbents toward Fe(III) sorption.

Sorbent	Temperature	pH	q mmol g^{-1}	Reference
5-IOW	25	4.0	0.155	[82]
14-IOW	25	4.0	0.116	[82]
Modified Mg-Al Layered double hydroxide	25	6.7	0.162	[83]
Spherical mesoporous silica (MCM-14)	25	7.0	0.031	[84]
Reference Clay-biochar composite 298 6.1	25	6.1	0.0899	[85]
SiO_2-G1.0	25	4.0	0.45	[62]
SiO_2-G2.2	25	4.0	0.62	[62]
SiO_2-G2.4	25	6.5	0.4	[62]
(acrylonitrile-co-acroleic acid-co-diaminopyridine) Nanofibrous film chemosensor	25	4.0	0.249	[86]
Silica gel-based sorbent (SiO_2@Nap)	25	4.0	1.414	[87]
TiO_2-banana cluster	25	4.0	2.686	[88]
CHI:L	22 (±1)	3.0	1.6	This work
CHI:UV	22 (±1)	3.0	2.1	This work
CH-AS:L	22 (±1)	3.0	4.551	This work
CH-AS:UV	22 (±1)	3.0	5.117	This work

2.2.4. Desorption and Sorbent Recycling

This stage is one of the most challenging parameters for designing the sorption process, which was described through the desorption of the bounded ions and the regeneration of the sorption. The elution was used through an acidic type of hydrochloric acid (0.5 M HCl solution). The suggestion of using acidic solutions for desorption of iron (III) from loaded sorbent is due to its proficiency to test the stability of the sorbent (chemically) and the sorption effectiveness (during the stability of recycling).

The desorption kinetics was investigated; Table 6 reports the loss in the sorption desorption capacities through five successive cycles, which indicates the stability in sorption with limited loss (around 4% from the total sorption), while the desorption is stable during the five cycles. It is worth noting that the complete desorption was achieved within 20 min (Figure 6), which means that it is faster than uptake.

Table 6. Average of sorbent (SE, %) /desorption (DE, %) recycles (from three repeated experiments) efficiencies for Fe(III) using the CH-AS for five cycles.

Metal Ion		Fe(III)	
Cycle	**Av./St. D**	**SE**	**DE**
1	Av. St. D.	81.6 0.65	100 0.34
2	Av. St. D.	81.4 0.34	100 0.42
3	Av. St. D.	80.95 0.25	100 0.37
4	Av. St. D.	80.15 0.33	100 0.51
5	Av. St. D.	79.8 0.23	99.9 0.22

Av.: average; St. D.: standard deviation (%).

The stability in the desorption efficiency is observed to be fixed at around 100%. However, the sorption efficiency is slightly declined at the fifth cycle by a percent that did not exceed 2.2%. This means the sorbent structure is remarkably stable for re-use. This is verified by the FTIR observations (Figure 2), which indicate restoration in the sorbent bands after desorption.

2.3. Effect of Light Mechanism on Fe(III) Sorption

The maximum sorption of both functionalized and nonfunctionalized sorbents was performed at acidic pH values, and the sorption performances (both sorbents) were improved by the UV condition. In which, at the pH of experimental sorption (pH_{eq} close to 3.1), the functional groups (amino, sulfonic, and hydroxyls) of the sorbent become partially protonated. These groups are considered the activated sites for binding with Fe(III) ions [89]. In the light-irradiation, the Fe particles were excited due to the presence of photonic energy (hv), leading to the liberation of electrons to form electron-lone pairs ($h^+ e^-$) (Equation (1)). This pair of electrons are moved to the iron surface to be involved in the redox reactions. The interaction of h^+ with water or hydroxyl yields radicals of ($^{\bullet}OH$) and consequently increases the H^+ in the solution (Equation (2)). This enhances the replacement between Fe(III) and H^+.

$$Fe \overset{hv}{\rightarrow} h^+ + e^- \quad (1)$$

$$h^+ + H_2O \text{ or } OH^- \rightarrow {}^{\cdot}OH + H^+ \quad (2)$$

2.4. The Study Area and Sampling Site

The water samples were collected from a 1200 m deep drilled well (Figure 8). The latitude and longitude coordinates are 28°19′31″ N and 28°48′44″ E, respectively, to the south of the Bawiti City (capital of the Bahariya Oasis). The Bahariya Oasis is one of the most prominent features in the Western Desert. It is a vast, natural, and deep depression located approximately 370 km southwest of Cairo in the heart of the Western Desert. The Bahariya Oasis has an oval shape in the general view, and its long axis is about 94 km, structurally orientated in a NE-SW direction, latitudes 27°46′27″ and 28°30′32″ N and longitudes 28°29′22″and 29°08′35″ E. The area is characterized by a hyper-arid climate

condition with rare rainfall that ranges from 3 to 6 mm/yr coupled with a very high evaporation rate. The Bahariya Oasis is linked to the Nile Valley by two main roads. The first road connects Giza to Bawiti cities, and the second road links Samalut City to the north of the El-Gedida iron ore mine. The two roads extend for 350 km and 220 km, respectively. The occurrence of springs and artesian wells from the Nubian Sandstone Aquifer System (NSAS) has paved the way for the settlement of humans since prehistoric times.

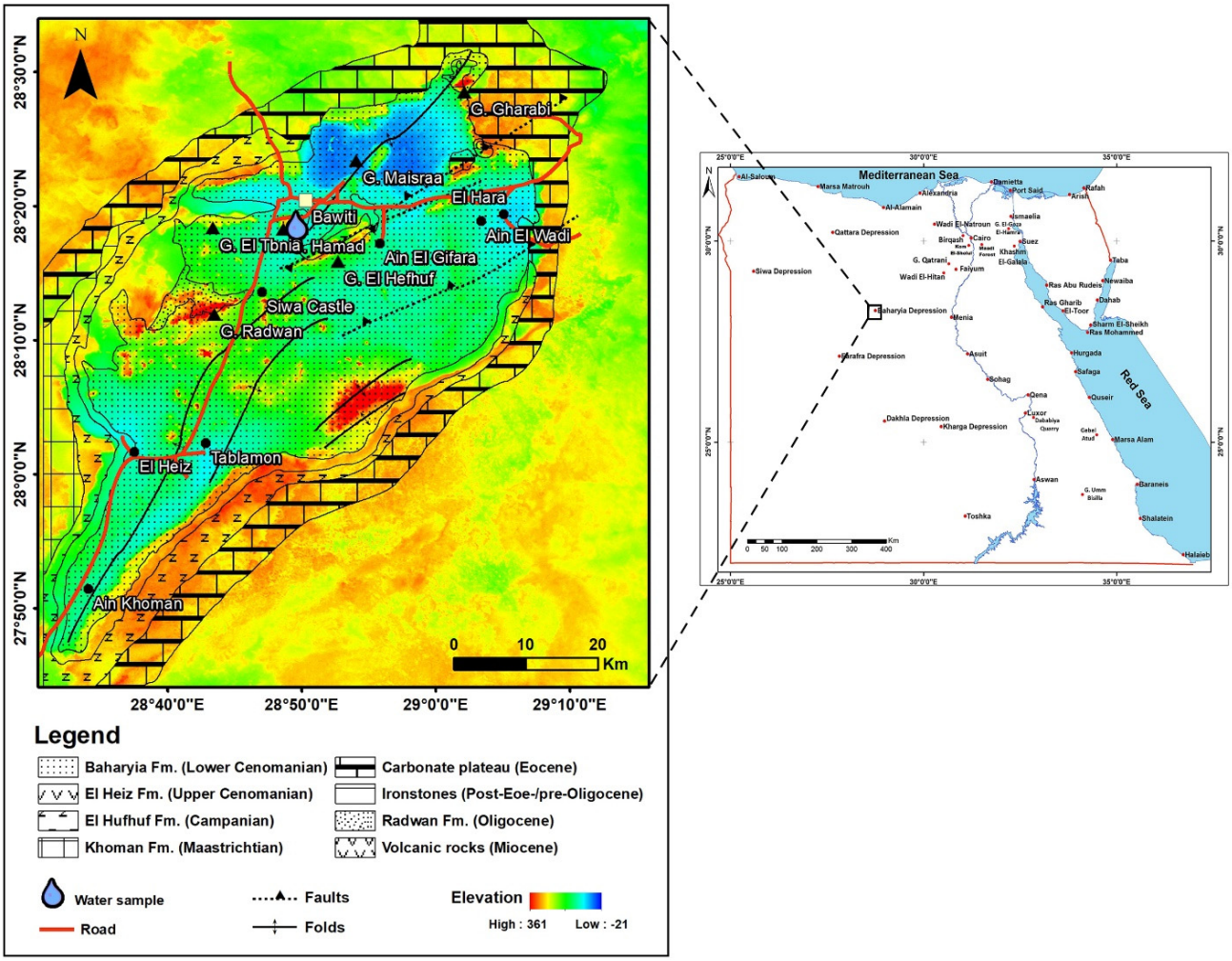

Figure 8. Geologic map of the Bahariya Oasis modified after [90].

2.5. Geology and Hydrogeology of the Studied Area

Geologically, the floor of the Bahariya Oasis (Figure 8) is generally flat and covered by the Cenomanian clastic rocks of the Bahariya Formation, whereas the flanks consist of Campanian, Maastrichtian, and Lower Eocene rocks. The Paleocene rocks are completely unrepresented in the Bahariya Oasis or its surrounding scarps. Scattered bushes are occasionally present on the ground. Sand dunes occupy small areas in the depression, e.g., Ghard Bawiti (5 km south Bawiti), Ghard Mandisha (south Mandisha Village), around Ain El Heiz, at the slopes of Gebel El-Hefhuf, and many others [91,92]. Aeolian sands and lacustrine deposits, and occasionally recent continental sabkhas form the Quaternary sediments. The Cretaceous succession can be distinguished from base to top in the Bahariya, El-Heiz, El-Hefhuf, Ain-Giffara, and Khoman Chalk formations [90,93,94]. The sedimentary sequence is intruded by sills and dykes of the Tertiary dolerites.

The north of the Bahariya Oasis is marked by the Eocene limestone plateau that ranges in elevation from 200 to 370 m amsl [95]. It is differentiated into three formations from base to top the Naqb, the Qazzun, and the Hamra formations. The stratigraphy of

the Bahariya Oasis shows tectonic instability throughout Cretaceous—Eocene time. The geographic distribution of various rock units and stratigraphic gaps indicate the Bahariya paleogeographic evolution with time [96].

Locally, the water-bearing sequences are comprised of two major aquifers. The first one is the water-bearing sequence contained in the Nubian sandstone, while the other is the water-bearing sequence contained in the post-Nubian rocks. The Nubian Sandstone Aquifer System (NSAS) is the prime water-bearing horizon within the Bahariya Oasis. It is the oldest and largest aquifer underlying the post-Nubian aquifer system (PNAS), with low-permeability aquicludes in between [97–100]. The Nubian sandstone is a common term for sands, sandstones, clays, and shales that overlies the basement complex. The aquifer was charged by the local infiltration amid the past wet periods (pluvial periods), which terminated in the south almost 4000 years ago, while it ended in the northeastern Sahara about 8000 years ago [101–103]. The Nubian Sandstone Aquifer System (NSAS) is essentially made up of continental clastic sediments and sandstone with intercalations of shale and clay. The thickness of this aquifer varies from 317 m in the southwest to more than 1000 m in the northwest [104].

The subsurface successions in Bawiti area at the Bahariya Oasis can be divided into two distinctive aquifers; (a) the lower Nubian Sandstone Aquifer and the upper Nubian Sandstone Aquifer. The two aquifers are separated by sand and shale layers and topped by the surface cover. The saturated thickness ranges from 70 to 110 m in the upper Nubian Sandstone Aquifer [105]. However, the groundwater in the Bahariya Oasis is distinguished into three horizontal aquifer zones (lower, middle, and upper), with shale and clay among the three zones [99].

The Bahariya Formation overlies the Nubian sandstone [106]. The Nubian Sandstone Aquifer System (NSAS) attains a thickness of 1800 m in the Bahariya Oasis [107,108]. The groundwater flows in the northeasterly direction [109]. The potentiometric surface of the Nubian Sandstone Aquifer System (NSAS) has witnessed a dramatic decline in the water table since 1990, as a result of the intense exploitation of groundwater. The annual drawdown in the water table ranges from 0.44 to 0.88 m [104]. Over time, the drawdown of the Bahariya Oasis is anticipated to be significantly lowered from 3 m to 26 m with minimal water distribution throughout the upcoming 25 years [110].

2.6. Treatment of Mine Contaminated Water

For evaluation of the sorption performance and selectivity for the sorbent and the potential in the water purification process for real-life application, the functionalized sorbent was tested with highly contaminated groundwater samples.

The studied groundwater samples are characterized by a high concentration of Fe (177 mgL^{-1}), while the concentration of Mn reaches 1.4 mgL^{-1}, and that of Cd and Pb are 0.3 and 0.78 mgL^{-1}, respectively. The concentration of these elements, especially iron, is higher than the permissible limits of drinking water by 590, 28, 33.3, and 156, respectively, as reported in Table S2, and some major elements (i.e., Na, Ca, and Mg with concentrations of 594.8, 164.6, and 71.99, respectively). The loading experiments were performed at the original value and the optimum loading from the synthetic solution. Figure 9 shows the selectivity of the sorbent toward Fe vs. metals, while Figure S7 shows the $SC_{pb/Metal}$. From these data, a progressive increase in the SC is noticed as pH increases, including the increase in removal efficiency of the hazardous elements as pH increases (the original pH is higher than pH 3.5). The selectivity was measured for Fe against metal ions from the equation below:

$$\text{Selectivity coefficient SC} = \frac{D_{Fe}}{D_{metal}} = \frac{q_{eq}(Fe) \times C_{eq}(metal)}{C_{eq}(Fe) \times q_{eq}(metal)} \quad (3)$$

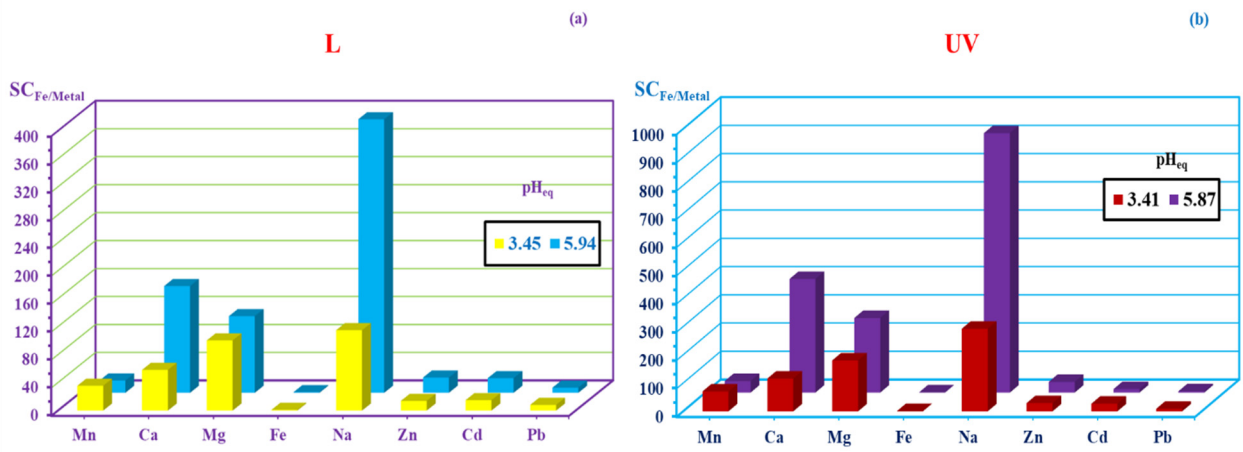

Figure 9. Selectivity coefficient for the functionalized sorbent for Fe(III) vs. associated metal ions at light (**a**) and UV (**b**).

From Figure 9, the order of SC can be arranged as Na >> Mg > Ca >> Mn > Cd ≈ Zn > Pb at pH_{eq} 3.4, while at pH_{eq} 5.94 the order changes to Na >> Ca > Mg >> Zn ≈ Cd ≈ Mn > Pb. In the case of UV application, the order of selectivity is Na>> Mg > Ca >> Mn > Zn ≈ Cd > Pb (at pH_{eq} 3.41) and Na >>> Ca > Mg >> Mn ≈ Zn > Cd > Pb (at pH_{eq} 5.87). This indicates the efficient use of UV over the light condition. The removal efficiency is shown in Figure 10. In addition, the selectivity was measured for the Pb against other elements.

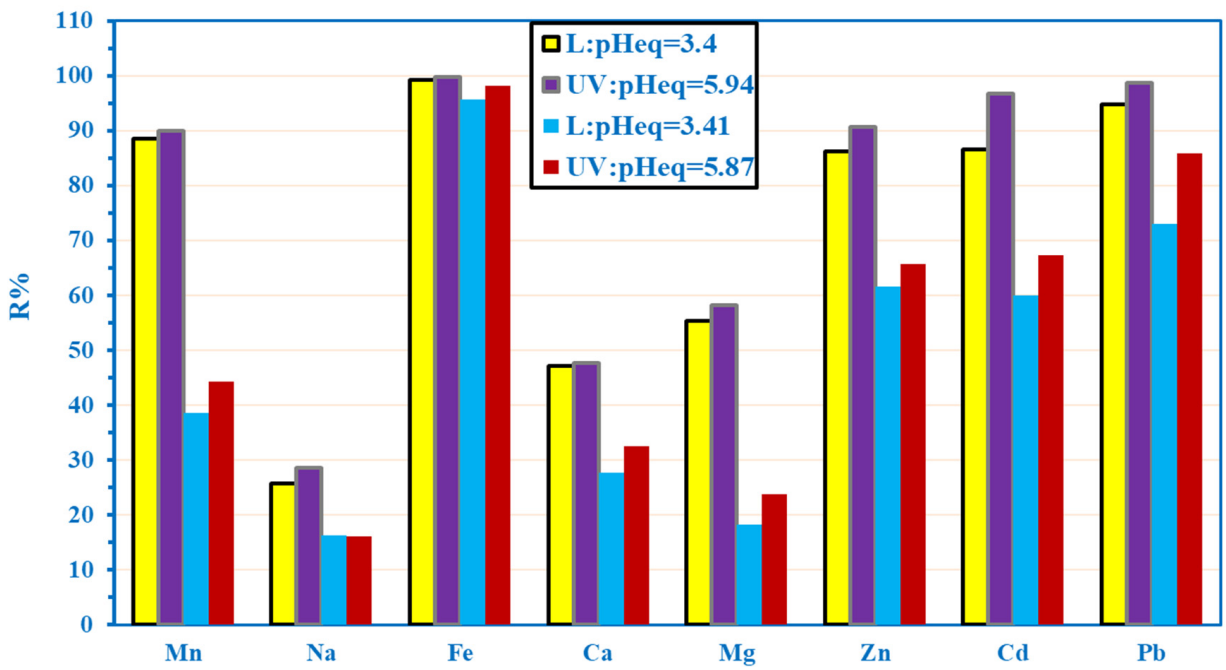

Figure 10. Removal efficiency (%) of ions in contaminated water under light and UV conditions.

3. Materials and Methods

3.1. Materials and Reagents

4-aminoazobenzene-3,4′-disulfonic acid (AZDS), glutaraldehyde solution (50 wt. %), chitosan (75–85% of acetylation degree (AD), medium molecular weight), acetic acid solution (≥99%), hydrate cadmium chloride ($CdCl_2.xH_2O$ (99%)), anhydrous calcium chloride (≥97%), ferric chloride ($FeCl_3{\cdot}6H_2O$ (97%)), aluminum chloride hydrate ($AlCl_3{\cdot}xH_2O$ (99.99%)), and copper chloride dihydrate ($CuCl_2.2H_2O$ (99.999%)) were purchased from the Sigma Aldrich (Darmstadt, Germany). Magnesium chloride hexahydrate ($MgCl_2{\cdot}6H_2O$

(99.9%)), zinc chloride ($ZnCl_2$ (98%)), and lead sulfate ($PbSO_4$) that were used in the selectivity experiments were obtained from Guangdong Guanghua, Sci-Tech Co., Ltd. (Guangdong, China). The solutions (synthetic/prepared solutions) were achieved by dilution from the stock of 1000 ppm metal ions solutions. Additionally, the deionized water was used in the preparation of the stock and diluted solutions for adsorption tests.

3.2. Synthesis of the Sorbents (CH and CH-AS)

The reaction of 5 g chitosan (after dissolution in 250 mL 6–7%; *w*/*w* of acetic acid) was reacted with 12.5 mL of GA solution to produce the chitosan crosslinked composite (CH; Scheme 1a; for comparing the sorption performance), while the reaction of 5 g chitosan (after dissolution as mentioned above) with 6 g of 4-aminoazobenzene-3,4′-disulfonic acid (after dissolution in 50 mL DMF solution) in the presence of 25 mL GA solution (for functionalized chitosan hydrogel Scheme 1b). The reactions (of both cases) were maintained at 75 °C for 9 h. The produced precipitates (CH and CH-AS) were filtered off and washed several times with water and ethanol before drying in vacuum at 60 °C for 10 h. The produced sorbents were used for loading and investigation of contaminated water treatment processes. Scheme 1a,b shows the synthetic route of both sorbents with a demonstration of the functional groups.

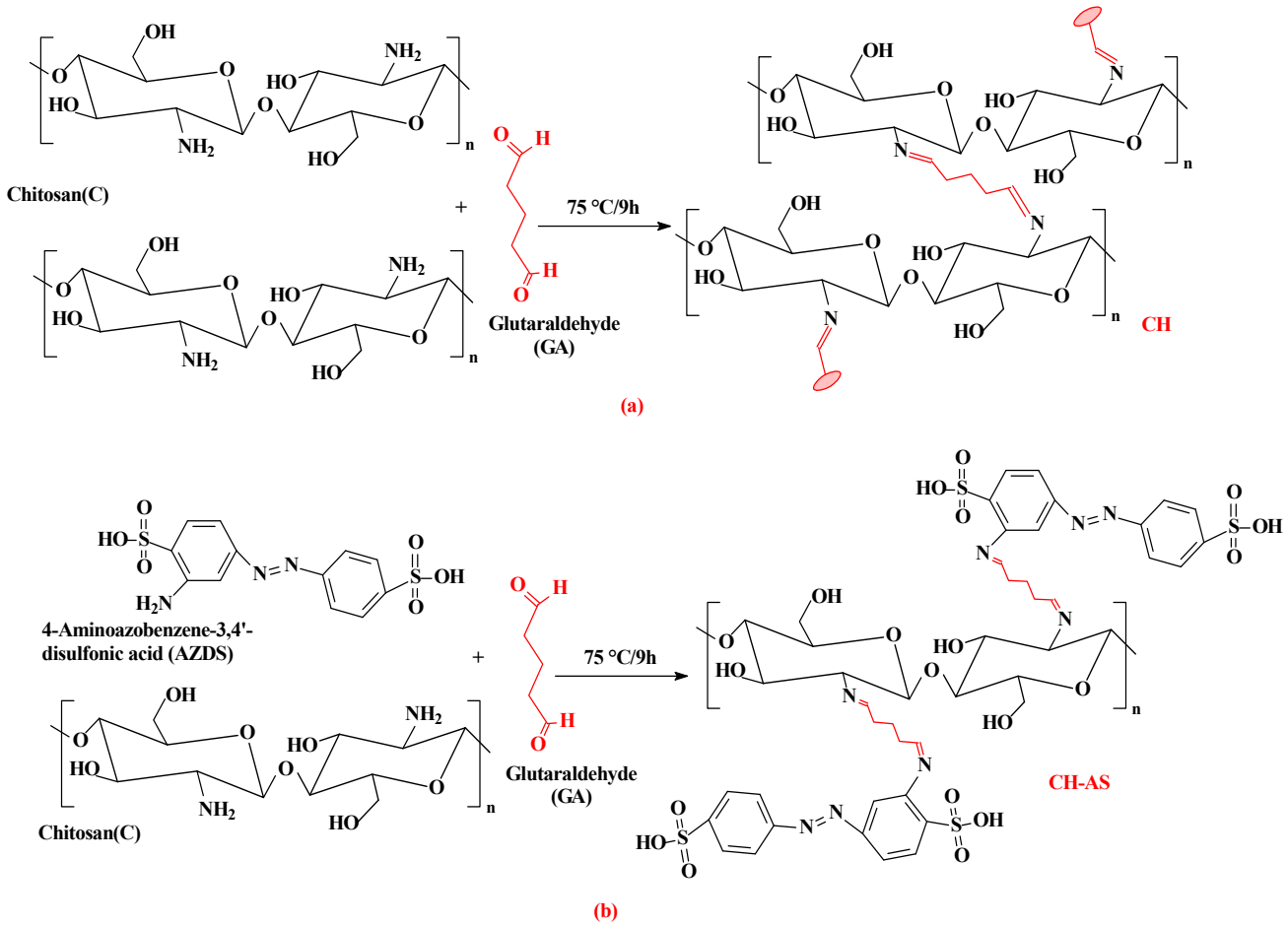

Scheme 1. Synthesis of crosslinked chitosan; CH (**a**) and functionalized sulfonic group composite; CH-AS (**b**).

3.3. Characterization

The synthesized materials (CH and CH-AS) were applied to verify the functionalization using FTIR spectrometry (confirmation of the reaction routes and successive grafting of sulfonic groups). This was performed after conditioning in the form of KBr pellets using

an IRT-racer, 100 FTIR spectrometer (Shimadzu, Kyoto, Japan). The determination of (C, H, N, S, and O) was conducted using elemental analyses by an element analyzer; CHNOS-Vario EL III- Elementar Analysensysteme-GmbH, Sonaustraβe, Germany. The thermal decomposition was verified by thermogravimetric analysis using Netzsch-STA, 449 F3 Jupiter-NETZSCH, Gerätebau, HGmbh, Selb, Germany. The analysis was performed under the nitrogen condition with 10 °C min^{-1} as a temperature ramp. SEM-EDX (scanning electron microscope, coupled with energy dispersive X-ray diffraction) analysis was carried out by using Quanta-FEG-200 (Thermo Fisher Scientific Merignac-FEI France) equipped with the Oxford Inca-350-EDX microanalyzer (Oxford Instruments; Saclay, France). PH-drift method [111] was used to describe the pH zero charge (pH_{pzc}). The adjusted and the varied pH were recorded in the solution after sorption using pH ionometer-S220 Seven; Mettler, Toledo-China. The photocatalytic sorption was studied using a 980-CW diode laser; Lambda Wave-Wrocław-Poland. The power of light is around 0.84-W, and the beam size is close to 8 mm^2. On the other hand, visible light was detected using the sunlight effect.

3.4. Sorption Studies

The study of sorption properties is achieved through batch systems as follows: a fixed weight amount (m, g) of sorbent was mixed with a fixed volume (V, L) of the solution under agitation speed v: 210 rpm at room temperature (22 ± 1 °C). The dose of the sorbent was adjusted to 0.5 g L^{-1} in most of the experiments. The pH (in the pH effect) varied from 1 to 3.5 (before precipitation point), in which the pH was not fixed (or controlled) during the sorption, but the initial and final pH were recorded. A fixed time (24 h) was set for the equilibrium experiments in the sorption isotherms, selectivity tests, etc. For the sorption isotherms, the concentration (initial conc C_0, mmol L^{-1}) of Fe(III) varied between 0.1 and 9.0 mmol Fe L^{-1} at pH 3.0. The selectivity experiment was used with the equimolar concentration of multi-component solutions at varied pH values (1–3) with a concentration of 1 mol metal L^{-1} of Cu(II), Ca(II), Zn(II), Mg(II), Al(III), Fe(III), and U(VI), at pH_0: 1.0, 1.99, and 2.95. In the case of uptake kinetics, the initial pH was set to 2 with an initial concentration of (C_0; 0.7 mmol Fe L^{-1}), and the samples were collected at different times by filtration of the sorbent before analyzing of the metal residual in the solution using ICP-AES. The amount of metal ions bounded on the sorbent (known as sorption capacity) (q, mmol g^{-1} or mg g^{-1}) was measured through the mass balance equation: $q = (C_0 - C_{eq}) \times V/m$, while the distribution ratio (D, L g^{-1}) is determined through $D = q_{eq}/C_{eq}$. The application to water samples was performed by testing 2 g of composite (m, g) with 1 L of the water sample (V, L). The bottles were constantly agitated for 1, 5, 10, and 24 h. After sorption, the sorbent was collected by filtration, and the residual metal content (C_{eq}, mmol L^{-1} or mg L^{-1}) was in the filtrate. It was measured using ICP-AES for evaluation of the sorption performances. The desorption was performed on the metal-loaded sorbents in an agitation system with a contact time of 24 h using 250 mL of 0.5 M HCl solutions (brought from kinetic experiments). Another experiment was performed to evaluate the sorbent stability by using five cycles of sorption and desorption. The analysis was performed on the eluate solution using ICP-AES to evaluate desorption performances. The FTIR spectra of the sorbents were exposed after five successive sorption/desorption cycles for sorbent stability through long-term uses. The models that are used in the fitting of the experimental profiles (for kinetic and isotherms) are summarized in Table S1a,b, respectively.

4. Conclusions

A new grafting of sulfonic groups was performed on chitosan magnetite nanoparticles to improve binding with heavy metal ions (through test of Fe(III)) on the sulfonic and amine functional groups. The sorption performances were investigated through different pH values compared with reference material. The maximum sorption was performed at pH around 3.5 with fast kinetic (the equilibrium attained in around 25 min). Improving the sorption of the functionalized material by using the UV emission not only increases the loading capacity from 2.7 to 3.06 mmol Fe g^{-1} but also enhances the sorption kinetics

by accelerating the sorption uptake from 35 min to less than 30 min. The sorption kinetics were fitted with PFORE, while the Langmuir and Sips equations were fitted for the sorption isotherms. The complete desorption was performed faster than sorption using a 0.2 M HCl solution.

Decontamination of groundwater from the Bahariya Oasis, Western Desert—Egypt, close to iron-mineralized area. The sorbent shows a high efficiency for removal of heavy metal ions even in the concentrations that are higher of the permissible limits by several hundred times, according to the drinking water or livestock drinking water of the World Health Organization (WHO). The efficient sorption allows the effluents that mainly fit for the livestock and irrigation purposes but slightly exceed the drinking water permissible limits. From the obtained sorption data, the current multifunctional materials offer a convenient and successful tool for developing the water purification processes in desert and mining areas.

Supplementary Materials: The following supporting information can be downloaded at: https://www.mdpi.com/article/10.3390/catal12070721/s1, Table S1a: Reminder of the equations used for modeling uptake kinetics [79–81]; Table S1b: Reminder of the equations used for modeling sorption isotherms [79,112,113]; Table S2: Comparison study of initial and final concentrations of metal ions on water sample before and after sorption; Figure S1: FTIR characterization of CH, CH-AS, after loading by Fe(III) and after the 5th cycles of sorption desorption (scale 400–1800 and 2800–4000 cm^{-1}); Figure S2: DrTGA of the functionalized chitosan composite; Figure S3: pH variation of the CH (a) and CH-AS (b) in the presence of Light and UV; Figure S4: Uptake kinetics; PSORE (a) and RIDE (b) at light and UV emission; Figure S5: Sorption isotherms for unfitting of the experimental data of Fe(III) sorption by Freundlich at light (a) and UV effect (b); Figure S6: Desorption kinetics of the functionalized sorbent for three repeated experiments; Figure S7: Selectivity coefficient for functionalized sorbent for Pb(II) vs. associated metal ions at light (a) and UV (b).

Author Contributions: Conceptualization, M.F.H., Y.W. and N.M.M.; methodology, M.F.H. and N.M.M.; software, S.H.A. and Y.W.; validation, M.F.H. and N.M.M.; formal analysis, investigation, and resources, M.F.H., Y.W., and N.M.M.; data curation, M.F.H. and S.H.A.; writing—original draft preparation, M.F.H. and N.M.M.; writing—review and editing, M.F.H. and N.M.M.; visualization, Y.W. and N.M.M.; project administration, S.H.A. and Y.W.; funding acquisition, S.H.A. and Y.W. All authors have read and agreed to the published version of the manuscript.

Funding: This research was funded by Taif University for Researchers Supporting Project (TURSP-2020/83), Taif University, Saudi Arabia.

Data Availability Statement: Data are available from the authors.

Acknowledgments: We acknowledge Taif University for the Researchers Supporting Project (TURSP-2020/83), Taif University, Saudi Arabia.

Conflicts of Interest: The authors declare no conflict of interest.

References

1. Shiklomanov, I.A. The world's water resources. In *Proceedings of the International Symposium to Commemorate*; UNESCO: Paris, France, 1991; pp. 93–126.
2. Shiklomanov, I.A.; Rodda, J.C. *World Water Resources at the Beginning of the Twenty-First Century*; Cambridge University Press: Cambridge, UK, 2004.
3. Boretti, A.; Rosa, L. Reassessing the projections of the World Water Development Report. *NPJ Clean Water* **2019**, *2*, 15. [CrossRef]
4. Leal Filho, W.; Totin, E.; Franke, J.A.; Andrew, S.M.; Abubakar, I.R.; Azadi, H.; Nunn, P.D.; Ouweneel, B.; Williams, P.A.; Simpson, N.P. Understanding responses to climate-related water scarcity in Africa. *Sci. Total Environ.* **2022**, *806*, 150420. [CrossRef] [PubMed]
5. Ahmed, M.; Sultan, M.; Wahr, J.; Yan, E. The use of GRACE data to monitor natural and anthropogenic induced variations in water availability across Africa. *Earth-Sci. Rev.* **2014**, *136*, 289–300. [CrossRef]
6. Ahmed, M.; Wiese, D.N. Short-term trends in Africa's freshwater resources: Rates and drivers. *Sci. Total Environ.* **2019**, *695*, 133843. [CrossRef]
7. Mekonnen, M.M.; Hoekstra, A.Y. Four billion people facing severe water scarcity. *Sci. Adv.* **2016**, *2*, e1500323. [CrossRef] [PubMed]

8. FAO; UNICEF; WFP; WHO. *The State of Food Security and Nutrition in the World 2019. Safeguarding against Economic Slowdowns and Downturns*; FAO: Rome, Italy, 2020; pp. 1–239.
9. WHO. *World Health Statistics 2018: Monitoring Health for the SDGs, Sustainable Development Goals*; World Health Organization: Geneva, Switzerland, 2018.
10. Heggy, E.; Sharkawy, Z.; Abotalib, A.Z. Egypt's water budget deficit and suggested mitigation policies for the Grand Ethiopian Renaissance Dam filling scenarios. *Environ. Res. Lett.* **2021**, *16*, 074022. [CrossRef]
11. El Bedawy, R. Water resources management: Alarming crisis for Egypt. *J. Mgmt. Sustain.* **2014**, *4*, 108. [CrossRef]
12. *Central Agency for Public Mobilization and Statistics (CAPMAS) Released Statistical Yearbook*; CAPMAS: Cairo, Egypt, 2020.
13. Egypt, M. *Water Challenges in Egypt*; Online Pamphlet; Ministry of Water Resources and Irrigation: Giza Governorate, Egypt, 2010.
14. Gleeson, T.; Befus, K.M.; Jasechko, S.; Luijendijk, E.; Cardenas, M.B. The global volume and distribution of modern groundwater. *Nat. Geosci.* **2016**, *9*, 161–167. [CrossRef]
15. Richter, B.; Kreitler, C. *Geochemical Techniques for Indentifying Sources of Groundwater Salinization*; CK Smoley: Boca Katon, FL, USA, 1993; Volume 258.
16. Prior, J.C.; Boekhoff, J.L.; Howes, M.R.; Libra, R.D.; VanDorpe, P.E. *Iowa's Groundwater Basics: A Geological Guide to the Occurence, Use, and Vulnerability of Iowa's Aquifers*; National Academy of Sciences: Washington, DC, USA, 2003.
17. Mashaal, N.; Akagi, T.; Ishibashi, J. Hydrochemical and isotopic study of groundwater in Wadi El-Natrun, Western Desert, Egypt: Implication for salinization processes. *J. Afr. Earth Sci.* **2020**, *172*, 104011. [CrossRef]
18. Hem, J.D. Study and interpretation of the chemical characteristics of natural water. In *US Geological Survey Water-Supply Paper 2254*, 3rd ed.; United States Government Printing Office: Washington, DC, USA, 1985.
19. Sawyer, C.N.; McCarty, P.L. *Chemistry for Sanitary Engineers*; McGraw, Hill Book Company: New York, NY, USA, 1967.
20. Khozyem, H.; Hamdan, A.; Tantawy, A.A.; Emam, A.; Elbadry, E. Distribution and origin of iron and manganese in groundwater: Case study, Balat-Teneida area, El-Dakhla Basin, Egypt. *Arab. J. Geosci.* **2019**, *12*, 523. [CrossRef]
21. WHO. *Guidelines for Drinking-Water Quality*; WHO: Geneva, Switzerland, 2011; Volume 216, pp. 303–304.
22. Fouda, A.; Eid, A.M.; EL-Belely, E.F.; Awad, M.A.; Hassan, S.E.-D.; AL-Faifi, Z.E.; Hamza, M.F. Enhanced antimicrobial, cytotoxicity, larvicidal, and repellence activities of phyco-synthesized magnesium oxide nanoparticles using brown algae, Cystoseira crinita. *Front. Bioeng. Biotechnol.* **2022**, *10*, 849921. [CrossRef] [PubMed]
23. Kavak, D. Removal of lead from aqueous solutions by precipitation: Statistical analysis and modeling. *Desalination Water Treat.* **2013**, *51*, 1720–1726. [CrossRef]
24. Zhizhaev, A.M.; Merkulova, E.N.; Bragin, I.V. Copper precipitation from sulfate solutions with calcium carbonates. *Russ. J. Appl. Chem.* **2007**, *80*, 1632–1635. [CrossRef]
25. Matlock, M.M.; Howerton, B.S.; Atwood, D.A. Irreversible precipitation of mercury and lead. *J. Hazard. Mater.* **2001**, *84*, 73–82. [CrossRef]
26. Hamza, M.F.; Roux, J.-C.; Guibal, E. Metal valorization from the waste produced in the manufacturing of Co/Mo catalysts: Leaching and selective precipitation. *J. Mater. Cycles Waste Manag.* **2019**, *21*, 525–538. [CrossRef]
27. Hamza, M.F.; El-Aassy, I.E.; Guibal, E. Integrated treatment of tailing material for the selective recovery of uranium, rare earth elements and heavy metals. *Miner. Eng.* **2019**, *133*, 138–148. [CrossRef]
28. Zhu, Z.W.; Pranolo, Y.; Cheng, C.Y. Uranium recovery from strong acidic solutions by solvent extraction with Cyanex 923 and a modifier. *Miner. Eng.* **2016**, *89*, 77–83. [CrossRef]
29. Jha, M.K.; Gupta, D.; Choubey, P.K.; Kumar, V.; Jeong, J.; Lee, J.-C. Solvent extraction of copper, zinc, cadmium and nickel from sulfate solution in mixer settler unit (MSU). *Sep. Purif. Technol.* **2014**, *122*, 119–127. [CrossRef]
30. Gavilan, K.C.; Pestov, A.V.; Garcia, H.M.; Yatluk, Y.; Roussy, J.; Guibal, E. Mercury sorption on a thiocarbamoyl derivative of chitosan. *J. Hazard. Mater.* **2009**, *165*, 415–426. [CrossRef]
31. Fadel, D.A.; El-Bahy, S.M.; Abdelaziz, Y.A. Heavy metals removal using iminodiacetate chelating resin by batch and column techniques. *Desalination Water Treat.* **2016**, *57*, 25718–25728. [CrossRef]
32. Hamza, M.F. Grafting of quaternary ammonium groups for uranium (VI) recovery: Application on natural acidic leaching liquor. *J. Radioanal. Nucl. Chem.* **2019**, *322*, 519–532. [CrossRef]
33. Hamza, M.F.; Fouda, A.; Wei, Y.; El Aassy, I.E.; Alotaibi, S.H.; Guibal, E.; Mashaal, N.M. Functionalized biobased composite for metal decontamination-Insight on uranium and application to water samples collected from wells in mining areas (Sinai). *Chem. Eng. J.* **2021**, *431*, 133967. [CrossRef]
34. Hamza, M.F.; Wei, Y.; Khalafalla, M.S.; Abed, N.S.; Fouda, A.; Elwakeel, K.Z.; Guibal, E.; Hamad, N.A. U (VI) and Th (IV) recovery using silica beads functionalized with urea-or thiourea-based polymers–Application to ore leachate. *Sci. Total Environ.* **2022**, *821*, 153184. [CrossRef] [PubMed]
35. Hamza, M.F.; Khalafalla, M.S.; Wei, Y.; Hamad, N.A. Effect of bi-functionalization silica micro beads on uranium adsorption from synthetic and washing pregnant uranyl solutions. *J. Radioanal. Nucl. Chem.* **2021**, *330*, 191–206. [CrossRef]
36. Pehlivan, E.; Altun, T. Ion-exchange of Pb^{2+}, Cu^{2+}, Zn^{2+}, Cd^{2+}, and Ni^{2+} ions from aqueous solution by Lewatit CNP 80. *J. Hazard. Mater.* **2007**, *140*, 299–307. [CrossRef]
37. Hamza, M.F.; Mubark, A.E.; Wei, Y.; Vincent, T.; Guibal, E. Quaternization of composite algal/PEI beads for enhanced uranium sorption—Application to ore acidic leachate. *Gels* **2020**, *6*, 12. [CrossRef]

38. Hamza, M.F. Removal of uranium (VI) from liquid waste of calcareous shale, Allouga, southwestern Sinai, Egypt. *Desalination Water Treat.* **2015**, *54*, 2530–2540. [CrossRef]
39. Hamza, M.F. Uranium recovery from concentrated chloride solution produced from direct acid leaching of calcareous shale, Allouga ore materials, southwestern Sinai, Egypt. *J. Radioanal. Nucl. Chem.* **2018**, *315*, 613–626. [CrossRef]
40. Zahra, M.H.; Hamza, M.F.; El-Habibi, G.; Abdel-Rahman, A.A.-H.; Mira, H.I.; Wei, Y.; Alotaibi, S.H.; Amer, H.H.; Goda, A.E.-S.; Hamad, N.A. Synthesis of a Novel Adsorbent Based on Chitosan Magnetite Nanoparticles for the High Sorption of Cr (VI) ions: A Study of Photocatalysis and Recovery on Tannery Effluents. *Catalysts* **2022**, *12*, 678. [CrossRef]
41. Dai, X.; Nhung, N.T.H.; Hamza, M.F.; Guo, Y.; Chen, L.; He, C.; Ning, S.; Wei, Y.; Dodbiba, G.; Fujita, T. Selective adsorption and recovery of scandium from red mud leachate by using phosphoric acid pre-treated pitaya peel biochar. *Sep. Purif. Technol.* **2022**, *292*, 121043. [CrossRef]
42. Hamza, M.F.; Hamad, N.A.; Hamad, D.M.; Khalafalla, M.S.; Abdel-Rahman, A.A.-H.; Zeid, I.F.; Wei, Y.; Hessien, M.M.; Fouda, A.; Salem, W.M. Synthesis of Eco-Friendly Biopolymer, Alginate-Chitosan Composite to Adsorb the Heavy Metals, Cd (II) and Pb (II) from Contaminated Effluents. *Materials* **2021**, *14*, 2189. [CrossRef] [PubMed]
43. Hamza, M.F.; Wei, Y.; Benettayeb, A.; Wang, X.; Guibal, E. Efficient removal of uranium, cadmium and mercury from aqueous solutions using grafted hydrazide-micro-magnetite chitosan derivative. *J. Mater. Sci.* **2020**, *55*, 4193–4212. [CrossRef]
44. Hamza, M.F.; Abdel-Rahman, A.A.H.; Guibal, E. Magnetic glutamine-grafted polymer for the sorption of U (VI), Nd (III) and Dy (III). *J. Chem. Technol. Biotechnol.* **2018**, *93*, 1790–1806. [CrossRef]
45. Wei, Y.; Salih, K.A.; Lu, S.; Hamza, M.F.; Fujita, T.; Vincent, T.; Guibal, E. Amidoxime functionalization of algal/polyethyleneimine beads for the sorption of Sr (II) from aqueous solutions. *Molecules* **2019**, *24*, 3893. [CrossRef] [PubMed]
46. Hamza, M.F.; Ahmed, F.Y.; El-Aassy, I.; Fouda, A.; Guibal, E. Groundwater purification in a polymetallic mining area (SW Sinai, Egypt) using functionalized magnetic chitosan particles. *Water Air Soil Pollut.* **2018**, *229*, 360. [CrossRef]
47. Vijayaraghavan, K.; Thilakavathi, M.; Palanivelu, K.; Velan, M. Continuous sorption of copper and cobalt by crab shell particles in a packed column. *Environ. Technol.* **2005**, *26*, 267–276. [CrossRef]
48. Mata, Y.N.; Blazquez, M.L.; Ballester, A.; Gonzalez, F.; Munoz, J.A. Biosorption of cadmium, lead and copper with calcium alginate xerogels and immobilized *Fucus vesiculosus*. *J. Hazard. Mater.* **2009**, *163*, 555–562. [CrossRef]
49. Wang, S.; Vincent, T.; Faur, C.; Guibal, E. Alginate and algal-based beads for the sorption of metal cations: Cu(II) and Pb(II). *Int. J. Mol. Sci.* **2016**, *17*, 1453. [CrossRef]
50. Hamza, M.F.; Fouda, A.; Elwakeel, K.Z.; Wei, Y.; Guibal, E.; Hamad, N.A. Phosphorylation of guar gum/magnetite/chitosan nanocomposites for uranium (VI) sorption and antibacterial applications. *Molecules* **2021**, *26*, 1920. [CrossRef]
51. Croisier, F.; Jérôme, C. Chitosan-based biomaterials for tissue engineering. *Eur. Polym. J.* **2013**, *49*, 780–792. [CrossRef]
52. Hamza, M.F.; Aly, M.M.; Abdel-Rahman, A.A.-H.; Ramadan, S.; Raslan, H.; Wang, S.; Vincent, T.; Guibal, E. Functionalization of magnetic chitosan particles for the sorption of U (VI), Cu (II) and Zn (II)—Hydrazide derivative of glycine-grafted chitosan. *Materials* **2017**, *10*, 539. [CrossRef] [PubMed]
53. Hamza, M.F.; Gamal, A.; Hussein, G.; Nagar, M.S.; Abdel-Rahman, A.A.H.; Wei, Y.; Guibal, E. Uranium (VI) and zirconium (IV) sorption on magnetic chitosan derivatives–effect of different functional groups on separation properties. *J. Chem. Technol. Biotechnol.* **2019**, *94*, 3866–3882. [CrossRef]
54. Yang, Z.; Chai, Y.; Zeng, L.; Gao, Z.; Zhang, J.; Ji, H. Efficient removal of copper ion from wastewater using a stable chitosan gel material. *Molecules* **2019**, *24*, 4205. [CrossRef] [PubMed]
55. Peniche, C.; Argüelles-Monal, W.; Goycoolea, F. *Chitin and Chitosan: Major Sources, Properties and Applications, Monomers, Polymers and Composites from Renewable Resources*; Elsevier: Amsterdam, The Netherlands, 2008; pp. 517–542.
56. Zargar, V.; Asghari, M.; Dashti, A. A review on chitin and chitosan polymers: Structure, chemistry, solubility, derivatives, and applications. *ChemBioEng Rev.* **2015**, *2*, 204–226. [CrossRef]
57. Hamza, M.F.; Salih, K.A.; Zhou, K.; Wei, Y.; Khoziem, H.A.A.; Alotaibi, S.H.; Guibal, E. Effect of bi-functionalization of algal/polyethyleneimine composite beads on the enhancement of tungstate sorption: Application to metal recovery from ore leachate. *Sep. Purif. Technol.* **2022**, *290*, 120893. [CrossRef]
58. Ashrafizadeh, M.; Mohammadinejad, R.; Kailasa, S.K.; Ahmadi, Z.; Afshar, E.G.; Pardakhty, A. Carbon dots as versatile nanoarchitectures for the treatment of neurological disorders and their theranostic applications: A review. *Adv. Colloid Interface Sci.* **2020**, *278*, 102123. [CrossRef]
59. Hamza, M.F.; Abdel-Rahman, A.A.-H. Extraction studies of some hazardous metal ions using magnetic peptide resins. *J. Dispers. Sci. Technol.* **2015**, *36*, 411–422. [CrossRef]
60. Wang, L.; Hu, D.; Kong, X.; Liu, J.; Li, X.; Zhou, K.; Zhao, H.; Zhou, C. Anionic polypeptide poly (γ-glutamic acid)-functionalized magnetic Fe3O4-GO-(o-MWCNTs) hybrid nanocomposite for high-efficiency removal of Cd (II), Cu (II) and Ni (II) heavy metal ions. *Chem. Eng. J.* **2018**, *346*, 38–49. [CrossRef]
61. Aguila, B.; Sun, Q.; Perman, J.A.; Earl, L.D.; Abney, C.W.; Elzein, R.; Schlaf, R.; Ma, S. Efficient mercury capture using functionalized porous organic polymer. *Adv. Mater.* **2017**, *29*, 1700665. [CrossRef]
62. Li, H.; Niu, Y.; Xue, Z.; Mu, Q.; Wang, K.; Qu, R.; Chen, H.; Bai, L.; Yang, H.; Wei, D. Adsorption property and mechanism of PAMAM dendrimer/silica gel hybrids for Fe (III) and Ag (I) from N, N-dimethylformamide. *J. Mol. Liq.* **2019**, *273*, 305–313. [CrossRef]
63. Piasek, Z.; Urbanski, T. The infra-red absorption spectrum and structure of urea. *Bull. Pol. Acad. Sci.* **1962**, *10*, 113–120.

64. Manivannan, M.; Rajendran, S. Investigation of inhibitive action of urea-Zn^{2+} system in the corrosion control of carbon steel in sea water. *Int. J. Environ. Sci. Technol.* **2011**, *3*, 8048–8060.
65. Jin, W.; Shen, D.; Liu, Q.; Xiao, R. Evaluation of the co-pyrolysis of lignin with plastic polymers by TG-FTIR and Py-GC/MS. *Polym. Degrad. Stab.* **2016**, *133*, 65–74. [CrossRef]
66. Coates, J. Interpretation of Infrared Spectra, A Practical Approach. In *Encyclopedia of Analytical Chemistry*; John Wiley & Sons, Ltd.: Hoboken, NJ, USA, 2006; pp. 1–23.
67. Zhang, Z.; Cao, Y.L.; Chen, L.N.; Huang, Z.Y. Preparation of thiol-functionalized cellulose and its application to the removal of Hg(II) from water environment. *Cellul. Chem. Technol.* **2017**, *51*, 559–567.
68. Chandra, S.; Saleem, H.; Sundaraganesan, N.; Sebastian, S. Experimental and theoretical vibrational spectroscopic and HOMO, LUMO studies of 1,3-dimethylbarbituric acid. *Ind. J. Chem.* **2009**, *48A*, 1219–1227.
69. Corazzari, I.; Nistico, R.; Turci, F.; Faga, M.G.; Franzoso, F.; Tabasso, S.; Magnacca, G. Advanced physico-chemical characterization of chitosan by means of TGA coupled on-line with FTIR and GCMS: Thermal degradation and water adsorption capacity. *Polym. Degrad. Stabil.* **2015**, *112*, 1–9. [CrossRef]
70. Lawrie, G.; Keen, I.; Drew, B.; Chandler-Temple, A.; Rintoul, L.; Fredericks, P.; Grondahl, L. Interactions between alginate and chitosan biopolymers characterized using FTIR and XPS. *Biomacromolecules* **2007**, *8*, 2533–2541. [CrossRef]
71. Duarte, M.L.; Ferreira, M.C.; Marvao, M.R.; Rocha, J. An optimised method to determine the degree of acetylation of chitin and chitosan by FTIR spectroscopy. *Int. J. Biol. Macromol.* **2002**, *31*, 1–8. [CrossRef]
72. Caetano, C.S.; Caiado, M.; Farinha, J.; Fonseca, I.M.; Ramos, A.M.; Vital, J.; Castanheiro, J.E. Esterification of free fatty acids over chitosan with sulfonic acid groups. *Chem. Eng. J.* **2013**, *230*, 567–572. [CrossRef]
73. Hamza, M.F.; Adel, A.-H.; Hawata, M.A.; El Araby, R.; Guibal, E.; Fouda, A.; Wei, Y.; Hamad, N.A. Functionalization of magnetic chitosan microparticles–Comparison of trione and trithione grafting for enhanced silver sorption and application to metal recovery from waste X-ray photographic films. *J. Environ. Chem. Eng.* **2022**, *10*, 107939. [CrossRef]
74. Hamza, M.F.; Salih, K.A.; Adel, A.-H.; Zayed, Y.E.; Wei, Y.; Liang, J.; Guibal, E. Sulfonic-functionalized algal/PEI beads for scandium, cerium and holmium sorption from aqueous solutions (synthetic and industrial samples). *Chem. Eng. J.* **2021**, *403*, 126399. [CrossRef]
75. Hamza, M.F.; Abdel-Rahman, A.A.-H.; Negm, A.S.; Hamad, D.M.; Khalafalla, M.S.; Fouda, A.; Wei, Y.; Amer, H.H.; Alotaibi, S.H.; Goda, A.E.-S. Grafting of Thiazole Derivative on Chitosan Magnetite Nanoparticles for Cadmium Removal—Application for Groundwater Treatment. *Polymers* **2022**, *14*, 1240. [CrossRef] [PubMed]
76. Hamza, M.F.; Goda, A.E.-S.; Ning, S.; Mira, H.I.; Abdel-Rahman, A.A.-H.; Wei, Y.; Fujita, T.; Amer, H.H.; Alotaibi, S.H.; Fouda, A. Photocatalytic Efficacy of Heterocyclic Base Grafted Chitosan Magnetite Nanoparticles on Sorption of Pb (II); Application on Mining Effluent. *Catalysts* **2022**, *12*, 330. [CrossRef]
77. Akkoz, Y.; Coskun, R.; Delibas, A. Preparation and characterization of sulphonated bio-adsorbent from waste hawthorn kernel for dye (MB) removal. *J. Mol. Liq.* **2019**, *287*, 11. [CrossRef]
78. Urbano, B.; Rivas, B.L. Poly(sodium 4-styrene sulfonate) and poly(2-acrylamido glycolic acid) polymer–clay ion exchange resins with enhanced mechanical properties and metal ion retention. *Polym. Int.* **2012**, *61*, 23–29. [CrossRef]
79. Tien, C. *Adsorption Calculations and Modeling*; Butterworth-Heinemann: Newton, MA, USA, 1994; p. 243.
80. Ho, Y.S.; McKay, G. Pseudo-second order model for sorption processes. *Process Biochem.* **1999**, *34*, 451–465. [CrossRef]
81. Crank, J. *The Mathematics of Diffusion*, 2nd ed.; Oxford University Press: Oxford, UK, 1975.
82. Fang, N.; He, Q.; Sheng, L.; Xi, Y.; Zhang, L.; Liu, H.; Cheng, H. Toward broader applications of iron ore waste in pollution control: Adsorption of norfloxacin. *J. Hazard. Mater.* **2021**, *418*, 126273. [CrossRef]
83. Khan, N.A.; Ahmed, S.; Farooqi, I.H.; Ali, I.; Vambol, V.; Changani, F.; Yousefi, M.; Vambol, S.; Khan, S.U.; Khan, A.H. Occurrence, sources and conventional treatment techniques for various antibiotics present in hospital wastewaters: A critical review. *TrAC Trends Anal. Chem.* **2020**, *129*, 115921. [CrossRef]
84. Hanna, N.; Sun, P.; Sun, Q.; Li, X.; Yang, X.; Ji, X.; Zou, H.; Ottoson, J.; Nilsson, L.E.; Berglund, B. Presence of antibiotic residues in various environmental compartments of Shandong province in eastern China: Its potential for resistance development and ecological and human risk. *Environ. Int.* **2018**, *114*, 131–142. [CrossRef]
85. Kuhlmann, J.; Dalhoff, A.; Zeiler, H.-J. *Quinolone Antibacterials*; Springer Science & Business Media: Berlin/Heidelberg, Germany, 2012.
86. Zhou, C.; Zhang, Y.; Liu, H. A novel nanofibrous film chemosensor for detecting and adsorbing Fe^{3+}. *J. Braz. Chem. Soc.* **2018**, *29*, 457–462. [CrossRef]
87. Chatterjee, S.; Gohil, H.; Paital, A.R. Dual functions of selective ferric ion detection and removal by a recyclable fluorescence active multifunctional silica material and toxic dye removal from aqueous solution. *ChemistrySelect* **2017**, *2*, 5348–5359. [CrossRef]
88. Wang, C.; Hu, T.; Wen, Z.; Zhou, J.; Wang, X.; Wu, Q.; Wang, C. Concentration-dependent color tunability of nitrogen-doped carbon dots and their application for iron (III) detection and multicolor bioimaging. *J. Colloid Interface Sci.* **2018**, *521*, 33–41. [CrossRef] [PubMed]
89. Mohamed, A.E.; Elgammal, W.E.; Eid, A.M.; Dawaba, A.M.; Ibrahim, A.G.; Fouda, A.; Hassan, S.M. Synthesis and characterization of new functionalized chitosan and its antimicrobial and in-vitro release behavior from topical gel. *Int. J. Biol. Macromol.* **2022**, *207*, 242–253. [CrossRef] [PubMed]
90. El Akkad, S.; Issawi, B. *Geology and Iron Ore Deposits of the Bahariya Oasis*; Paper 18; Geological Survey: Egypt, Cairo, 1963; p. 300.

91. Catuneanu, O.; Khalifa, M.A.; Wanas, H. Sequence stratigraphy of the lower cenomanian bahariya formation, bahariya oasis, western desert, Egypt. *Sediment. Geol.* **2006**, *190*, 121–137. [CrossRef]
92. Plyusnina, E.E.; Sallam, E.S.; Ruban, D.A. Geological heritage of the Bahariya and Farafra oases, the central Western Desert, Egypt. *J. Afr. Earth Sci.* **2016**, *116*, 151–159. [CrossRef]
93. Khalifa, M. Geological and Sedimentological Studies of El Hefhuf Area, Bahariya Oasis, Western Desert, Egypt. Master's Thesis, Cairo University, Cairo, Egypt, 1977.
94. Said, R. *The Geology of Egypt*; Elsevier Science Pub. Co.: Amsterdam, The Netherlands, 1962; Volume 377.
95. Said, R.; Issawi, B. *Geology of Northern Plateau, Bahariya Oasis, Egypt*; Paper 29; Geological Survey of Egypt: Cairo, Egypt, 1964.
96. Said, R. *The Geology of Egypt*; Routledge: London, UK, 2017.
97. Hamdan, A.M.; Sawires, R.F. Hydrogeological studies on the Nubian sandstone aquifer in El-Bahariya oasis, Western Desert, Egypt. *Arab. J. Geosci.* **2013**, *6*, 1333–1347. [CrossRef]
98. Sharaky, A.M.; Abdoun, S.H. Assessment of groundwater quality in Bahariya Oasis, Western Desert, Egypt. *Environ. Earth Sci.* **2020**, *79*, 145. [CrossRef]
99. *Rgional Strategy for the Utilization of the Nubian Sandstone Aquifer System*; Hydrogeolgy; CEDARE: Cairo, Egypt, 2001; Volume II.
100. Bakhbakhi, M. *Nubian Sandstone Aquifer System, Non-Renewable Groundwater Resources: A Guidebook on Socially Sustainable Management for Water-Policy Makers*; IHP-VI Series on Groundwater 10; United Nations Educational, Scientific and Cultural Organization: Paris, Frence, 2006; pp. 75–81.
101. Schneider, M. *Hydrogeologie des Nubischen Aquifersystems am Südrand des Dakhla-Beckens, Südägypten/Nordsudan*; Reimer: Berlin, Germany, 1986.
102. Hesse, K.-H.; Hissene, A.; Kheir, O.; Schnaecker, E.; Schneider, M.; Thorweihe, U. *Hydrogeological Investigations in the Nubian aquifer System, Eastern Sahara*; Dietrich Reimer: Berlin, Germany, 1987.
103. Heinl, M.; Thorweihe, U. Groundwater resources and management in SW Egypt. *Catena Suppl.* **1993**, *26*, 99–121.
104. Masoud, M.; El Osta, M. Evaluation of groundwater vulnerability in El-Bahariya Oasis, Western Desert, Egypt, using modelling and GIS techniques: A case study. *J. Earth Syst. Sci.* **2016**, *125*, 1139–1155. [CrossRef]
105. El Kashouty, M.; Aziz, A.A.; Soliman, M.; Mesbah, H. Hydrogeophysical investigation of groundwater potential in the El Bawiti, Northern Bahariya Oasis, Western Desert, Egypt. *Arab. J. Geosci.* **2012**, *5*, 953–970. [CrossRef]
106. Rabeh, T.; Bedair, S.; Abdel Zaher, M. Structural control of hydrogeological aquifers in the Bahariya Oasis, Western Desert, Egypt. *Geosci. J.* **2018**, *22*, 145–154. [CrossRef]
107. Hermina, M. The surrounding of Kharga, Dakhle and Farafra. In *Geology of Egypt*; Balkema: Leiden, The Netherlands, 1990.
108. Klitzsch, E.; Wycisk, P. *Beckenentwicklung und Sedimentationsprozesse in Kratonalen Bereichen Nordost-Afrikas im Phanerozoikum, Nordost-Afrika: Strukturen und Ressourcen: Ergebnisse aus dem Sonderforschungsbereich "Geowissenschaftliche Probleme in Ariden und Semiariden Gebieten"*; John Wiley & Sons, Inc.: Hoboken, NJ, USA, 1999; pp. 61–108.
109. Korany, E. On the demonstration of the hydrogeological control by local geologic structures, Bahariya Oasis, Egypt. In Proceedings of the EGS 3rd Annual Meeting, El Bahariya Oasis, Egypt, 1984; pp. 335–341.
110. El Hossary, M. Ensuring sustainable development via groundwater management (case study: El Bahariya Oasis). *J. Am. Sci.* **2013**, *9*, 6–13.
111. Lopez-Ramon, M.V.; Stoeckli, F.; Moreno-Castilla, C.; Carrasco-Marin, F. On the characterization of acidic and basic surface sites on carbons by various techniques. *Carbon* **1999**, *37*, 1215–1221. [CrossRef]
112. Langmuir, I. The adsorption of gases on plane surfaces of glass, mica and platinum. *J. Am. Chem. Soc.* **1918**, *40*, 1361–1402. [CrossRef]
113. Freundlich, H.M.F. Uber die adsorption in lasungen. *Z. Phys. Chem.* **1906**, *57*, 385–470.